

ENGINEERING
RESEARCH
ENGINEERING
RESEARCH

(NASA-CR-129178) NUMERICAL CALCULATIONS OF
FLOW FIELDS Progress Report, 1 Jul. 1971 -
30 Jun. 1972 D.M. Anderson, et al (Iowa
State Univ. of Science and Technology)
30 Jun. 1972 121 p

N73-11251

Unclas

CSSL 20D G3/12 16561

RESEARCH

ENGINEERING
RESEARCH
INSTITUTE

IOWA STATE
UNIVERSITY
AMES, IOWA

ENGINEERING
RESEARCH

ENGINEERING
RESEARCH

**ENGINEERING
RESEARCH**

**ENGINEERING
RESEARCH**

**ENGINEERING
RESEARCH**

**ENGINEERING
RESEARCH**

**ENGINEERING
RESEARCH**

PROGRESS REPORT

**NUMERICAL CALCULATIONS
OF FLOW FIELDS**

Dale Anderson and Jerry Vogel

1 July 1971 to 30 June 1972

Submitted to:

**NASA
Ames Research Center**

NGR 16-
**NASA Grant NGRIG-002-029
Project No. 911-S
ERI-72193**

**ENGINEERING RESEARCH INSTITUTE
IOWA STATE UNIVERSITY AMES**

Introduction

Iowa State University Engineering Research Institute Project 911-S is a continuation of NASA Grant NGRIG-002-029. The major areas of study and goals of this research project are:

- 1) Determine the flow field generated by a finitely thick lifting three-dimensional wing with subsonic tips moving at supersonic speeds.
- 2) Determine the flow field produced by a lifting elliptic cone using finite difference techniques.
- 3) Study the problem of cross-flow instability associated with lifting delta wing configurations such as space shuttle.

A six month extension of the current grant through December 1972 has been obtained in order to complete the first objective of the research project. Results obtained during the past year are presented through theses or reports where applicable.

1. Rectangular Wing Problem

The flow field associated with the forebody region of the symmetric rectangular wing has been determined for angles-of-attack of 0 and 4 degrees at a Mach number of 2. The original solution technique has been modified to include the entropy boundary conditions developed by Mike Abbett, thus replacing the reflection technique in the evaluation of the ultimate body values of the flow variables. Although the application of the boundary conditions as described by Abbett failed to yield a viable solution in the cone region (the wedge region solution was satisfactory) a suitable modification was made that did work. It would appear that in regions of small radius of curvature (in the cone-tip region) the predicted values of the velocity components on the body are not sufficiently accurate to use as inputs for the Abbett technique which would continuously expand the flow on the body. The modification consisted of using corrected body data obtained via reflection as inputs to the Abbett technique.

The flow field associated with the afterbody region of the rectangular wing is currently being developed. The forebody flow field data is transferred to the afterbody grid system at the wind midchord point, thus generating initial data for the afterbody. The integration technique and boundary conditions used are the same as for the forebody. To date, the integration has proceeded to a point approximately 90% of the distance back on the afterbody. In this region of the flow field on the body the cross flow eigenvalues grow rapidly as the trailing edge is encountered forcing the integration step size to be continuously decreased. Since the normal eigenvalues do not change appreciably along the afterbody the effective Courant number at which the solution is being obtained in the normal direction continuously decreases yielding a suboptimal solution in the normal direction in the region near the trailing edge of the wing. The situation has been improved somewhat by decreasing the number of grid points about the cone tip. It would appear that the afterbody solutions will be completed in the very near future.

The afterbody solutions will be used as initial data for the wake region integration. No problems are anticipated in the wake integration which should be completed shortly after the afterbody integration is furnished.

2) Elliptic Cone Flow Fields

Appendix A includes the thesis "Finite difference solutions to the equations of fluid flow around an elliptic cone" by Phil Pratt. This served as Phil's M.S. thesis and deals with the second part of the current effort.

The results presented compare favorably with both experimental and analytical data available. The only question arises when one notes the persistent oscillation in body pressure which occurs approximately 115° around the elliptic cones both at zero and non-zero angles of attack. This question should have been answered by a more complete investigation. However, the funds available for computer time and the time requirements precluded further investigation.

Since Pratt's work was completed, a new program has been written for solving the elliptic cone flow field. This has been done at the direction of the NASA Technical Monitor Dr. Kutler and will be used both in further studies of the elliptic cone and the cross-flow instability problem. This program is currently in the de-bug stages. A complete description of the new program will be presented in a later report when computed results are available.

3) Cross-Flow Instability Problem

The third part of the current effort is to study the problem of cross flow instability associated with very small radius of curvature areas such as the leading edge of the shuttle wing. This phase of the study will begin after the completion of the elliptic cone flow field study. The programs resulting from the elliptic cone study are necessary to the cross-flow investigation.

4) Other Work Partially or Wholly Supported Under the Current Grant

A) Numerical Advection Experiments

Appendix B is a paper which has been submitted to the Journal of Applied Meteorology for publication. This work was partially funded through the current grant and is included here. Behrooz Fattahi was the Graduate Assistant working on that particular paper.

B) Undefined Problems

Jim Daywitt has been supported by the current grant during the past year and will be starting on his thesis in September. His thesis topic is still undefined. It will be in an appropriate area dealing with finite difference methods in aerodynamics.

APPENDIX A

Finite difference solutions to the equations of
fluid flow around an elliptic cone

by

Philip Wayne Pratt

A Thesis Submitted to the
Graduate Faculty in Partial Fulfillment of
The Requirements for the Degree of
MASTER OF SCIENCE

Major: Aerospace Engineering

Approved:

In Charge of Major Work

For the Major Department

For the Graduate College

Iowa State University
Ames, Iowa

1972

TABLE OF CONTENTS

	Page
NOTATION	iv
SUMMARY	vii
INTRODUCTION	1
PROBLEM FORMULATION AND METHOD OF SOLUTION	5
Introduction	5
Coordinate System	6
Numerical Method	8
Initial Conditions	11
Boundary Conditions	12
Method of Solution	14
THE CIRCULAR CONE	17
THE ELLIPTIC CONE	22
Introduction	22
Zero Angle of Attack	24
Angle of Attack	26
ACKNOWLEDGEMENTS	28
BIBLIOGRAPHY	29
APPENDIX A: COORDINATE SYSTEM AND CONSERVATIVE EQUATIONS	44
Coordinate System	44
Conservative Equations	46
APPENDIX B: THE REFLECTION BOUNDARY CONDITION	48

	Page
APPENDIX C: THE ENTROPY BOUNDARY CONDITION	54
APPENDIX D: EIGENVALUES	62
APPENDIX E: NONDIMENSIONALIZATION AND INITIAL CONDITIONS	67
Nondimensionalization	67
Initial Conditions	67
APPENDIX F: INVERSION	68

NOTATION

A, B, C	Coefficient matrices of the gas dynamic equations
a	Semimajor axis of the body
b	Semiminor axis of the body
c	Characteristic length of the body
E, F, G, H	Matrices of conservative variables (Appendix A)
I	Identity matrix
$\hat{i}, \hat{j}, \hat{k}$	Unit vectors on the x, y, z directions
$\hat{i}_R, \hat{i}_N, \hat{i}_C$	Unit vectors in the radial, normal and cross flow directions
h_T	Total enthalpy
M	Mach number
P	Dimensionless pressure
\vec{q}	Dimensionless velocity vector
\vec{q}_i	Dimensionless velocity vector in the \vec{q}_i direction
\vec{R}	Radial vector (Figure 1)
r	Radius of circular cross section in computational system
S	Entropy
u, v, w	Dimensionless velocity components of \vec{q}
u_i^*, v_i^*, w_i^*	Dimensionless velocity components of \vec{q}_i^*
\vec{u}	Vector of independent flow variables
x, y, z	Coordinate directions in the physical Cartesian system
x', y', z'	Coordinate directions in the computational Cartesian system

α	Angle of attack
γ	Ratio of specific heats
$\Delta\beta$	Increment in the β -direction
$\Delta\delta$	Increment in the δ -direction
$\Delta\xi$	Increment in the ξ -direction
$\frac{\Delta\xi}{\Delta\delta}$	Mesh ratio
$\frac{\Delta\xi}{\Delta\beta}$	Mesh ratio
$\Delta\theta$	Angle through which flow is expanded or compressed (Appendix C)
ξ, δ, β	Coordinate directions in the computational polar system
ρ	Dimensionless density
σ, λ	Eigenvalues
∇	Vector operator

Subscripts:

c	Pertaining to the circular cone
C	Cross flow coordinate direction (Figure 1)
e	Pertaining to the elliptic cone
j	Mesh point in the δ -direction
k	Mesh point in the β -direction
max	Maximum
N	Coordinate direction normal to the body surface (Figure 1)
R	Radial coordinate direction (Figure 1)
tan	Tangential component

x, y, z	Partial derivatives with respect to x, y or z
x', y', z'	Partial derivatives with respect to x', y' or z'
1	Flow variables after the predictor
2	Flow variables after the corrector
∞	Freestream condition
ξ, δ, β	Partial derivative with respect to ξ, δ or β

Superscripts:

\sim	Predicted value of flow variables or intermediate matrix forms
n	Spacial step location in integration
$+, -$	Superlayer, sublayer
$-$	Dimensional quantity

SUMMARY

The solutions to the equations of motion for inviscid fluid flow around a pointed elliptic cone at incidence are presented. The numerical method used, MacCormack's second order preferential predictor-corrector finite difference approximation, is applied to the fluid flow equations derived in conservation-law form. The entropy boundary condition, hitherto unused for elliptic cone problems, is investigated and compared to reflection boundary condition solutions. The stagnation streamline movement of the inclined elliptic cone is noted and surface pressure coefficients are plotted.

Also presented are solutions for an elliptic cone and a circular cone at zero incidence and a circular cone at a small angle of attack. Comparisons are made between these present solutions and previously published theory.

INTRODUCTION

The reduction of complex bodies to simpler configurations in investigating aerodynamic characteristics has long been accepted practice. Leading edges of thin airfoils have been assumed to be wedges of finite (or infinite) span, and fuselages have been assumed to be circular cones attached to cylinders. These assumptions enabled the scientist/engineer to apply analytical methods to acquire solutions to the partial differential equations of fluid motion. However, as the aerodynamic "state of the art" grew, the configurations became more complex, and the "simplifying" bodies became more complicated. Therefore, it was necessary to seek improved and more efficient methods of solution.

The applicability of numerical methods to the solution of differential equations had been long known and understood, but it wasn't until the advent of the high-speed digital computer that efficient use could be made of these methods. Although these numerical approaches are quite amenable to many problem types, they should not be regarded as panaceas. Many times, more problems are created than solved with the introduction of the numerical techniques. Difficulties with numerical stability, accuracy, computer time and storage requirements, and applicability of the numerical methods to the physical situation often cause serious problems.

This paper is primarily concerned with the numerical solution to nonlinear conical flow and, in particular, the flow around elliptic cones at incidence. The circular cone has been the accepted configuration for modeling the supersonic flow about bodies of revolution for decades. However, for non-axisymmetric bodies immersed in a supersonic stream, the circular cone is of little use. Therefore, as Van Dyke (25) points out, the elliptic cone may become the model for these geometries. Furthermore, elliptic cones provide certain aerodynamic characteristics that surpass those of their circular counterpart (e.g., from Chapkis (7), greater L/D ratio for the same cross sectional area per unit height). Evidence of the impact of the elliptic geometry can easily be seen in present-day lifting body and space shuttle designs.

The problem of the supersonic flow field surrounding these bodies has been investigated by Ferri (8,9,10), Van Dyke (25), Melnick (19), Kahane and Solarski (13), Jones (12), Chapkis (7), and Martellucci (18), and others, with varying degrees of success. The papers by Ferri (10), Martellucci, Chapkis and Jones were of greatest assistance in this study, since they not only presented theoretical computations, but also numerical and experimental comparisons. The publications by Ferri (8,9), Van Dyke, and Kahane and Solarski were basically of theoretical content. Melnick's paper was of special interest, because it succinctly ex-

plained the streamline pattern and vortical singularity problems near the body.

South and Klunker (24) indicate two general approaches to the solution of nonlinear conical flows. The first includes the "distance asymptotic" methods, where initial conditions are chosen near the conical apex, and numerical integration proceeds downstream until conical similarity conditions (defined later) are satisfied. The second approach consists of "conical" methods that invoke the conical self-similarity, then reduce the problem to two independent variables. There are different variations to the approaches above: Rakich (22), Chapkis, Martellucci and Ferri utilize different forms of the method of characteristics; Kahane and Solariski propose Ward's elliptic slender body theory; and South and Klunker implement the method of lines (method of integral relations). For a brief history of these developments, the reader is referred to South and Klunker (24).

The method chosen for this study was the "distance asymptotic" method, utilizing a finite difference approach. However, this approach was modified slightly to enhance stability considerations. Instead of integrating downstream until convergence was attained, the integration was initiated at some point ξ , and a solution at some point $\xi + \Delta\xi$ was obtained. This solution was then used as the initial condition for another integration step at point ξ . A more de-

tailed explanation of the reasoning and procedure is presented later.

The elliptic body surface was defined mathematically, and boundary conditions were applied at the body surface and the unknown shock position. Freestream values for pressure, density, and velocities were used as initial conditions so that the numerical representation of the shock build-up was as if the cone had been impulsively started. However, the transient numerical flow field behind the shock may not represent the actual flow field until convergence has been attained.

The equations of fluid motion were simplified by assuming: 1) negligible viscosity, therefore eliminating boundary layer effects; 2) negligible heat conductivity; 3) a perfect gas; and 4) conical flow, resulting in isentropic flow along streamlines. The physical properties of conical flow are such that pressure, density, velocities, energy and entropy remain constant along rays emanating from the conical apex (i.e., the aforementioned conical similarity).

PROBLEM FORMULATION AND METHOD OF SOLUTION

Introduction

In the numerical solution of a flow problem, selection of the coordinate system, numerical technique, initial conditions, and boundary conditions is of prime importance. Although presented in a somewhat disjointed manner, these considerations are quite important. For example, the choice of a coordinate system may depend upon the manner in which the boundary conditions are applied and/or the numerical technique chosen. In turn, numerical stability and accuracy may depend on the manner in which the boundary conditions are employed and in the choice of coordinate system. Initial and boundary conditions are easier to derive if the coordinate system is as straightforward as possible. However, different coordinate systems have different eigenvalue structures and therefore different stability characteristics.

This section attempts to delineate the approach implemented in setting up the elliptic cone problem. To acquire a more complete understanding of this approach, frequent reference to the appendices is suggested. An attempt is made to keep this section free from lengthy, tedious derivations.

Coordinate System

The coordinate system chosen, shown in Figure 1, was the result of a double coordinate transformation. The first transformation, from the physical Cartesian system, (x, y, z) , to the computational Cartesian system, (x', y', z') , converted the elliptic cross section to a circular cross section (see Figure A-1). This constituted a stretching of the semimajor and semiminor axes, a and b , of the elliptic cone by a factor of b and a , respectively; provided $a, b \geq 0$.

As a result of this transformation, angles around the body in the y, z -plane were not conserved in the y', z' -plane. Evenly spaced angles around the computational Cartesian body produced rays that "clustered" about the $\beta = 90^\circ$ meridian in the physical plane (see Figure A-1). The relation governing the angles is given by:

$$\beta_e = \tan^{-1} \left[\frac{a}{b} \tan \beta_c \right], \quad (1)$$

where β_c is the computational plane body angle. This behavior is beneficial for elliptic cones of large eccentricities. For these cases, flow near the $\beta = 90^\circ$ meridian is of great importance due to the presence of large gradients in the flow variables. Using this transformation allows more mesh points to be concentrated in this area, therefore monitoring the

flow more closely.

The second transformation carried the computational Cartesian plane into the computational polar plane, (ξ, δ, β) , seen in Figure 1. This system allowed for the easy application of the elliptic boundary conditions to the circular cone (described in more detail later), while retaining the conical similarity of the flow field. For the numerical integration method chosen, requiring a coordinate axis to be coincident with the conical axis (i.e., $x = x' = \xi$) yielded simple functions of the gas dynamic variables in conservative form (see Equation 1-11). These functions could then be easily solved to yield explicit functions of the gas dynamic variables.

When the aforementioned assumptions (1) negligible viscosity; 2) negligible heat conductivity; 3) perfect gas; and 4) conical flow) were applied to the equations of motion of fluid flow, they yielded the following equations for consideration:

$$\text{X-Momentum: } (P + \rho u^2)_x + (\rho uv)_y + (\rho uw)_z = 0 \quad (2)$$

$$\text{Y-Momentum: } (\rho uv)_x + (P + \rho v^2)_y + (\rho vw)_z = 0 \quad (3)$$

$$\text{Z-Momentum: } (\rho uw)_x + (\rho vw)_y + (P + \rho w^2)_z = 0 \quad (4)$$

$$\text{Energy: } \vec{q} \cdot (\vec{\nabla} P - c^2 \vec{\nabla} \rho) = 0 \quad (5)$$

Continuity:

$$\nabla \cdot (\rho \vec{q}) = 0 \quad . \quad (6)$$

However, these equations are not yet in a form that will allow numerical computation. They must first be transformed to the computational polar coordinate system to be consistent with the geometry of the problem. Then, since the transformation gives rise to nonhomogeneous terms, the equations must be expanded to conservation-law form to accommodate the numerical method. This is done in Appendix A. For numerical significance, and as a matter of general practice, it is convenient to nondimensionalize the flow parameters. The nondimensionalization scheme used is presented in Appendix E.

Numerical Method

The numerical method chosen was MacCormack's (16) second order preferential predictor-corrector, utilizing a forward differencing predictor step and a backward differencing corrector step. This method was shown by Kutler (99) to be superior to first order and many second order methods in terms of computer time and storage, programming ease and accuracy. The method is a finite difference technique that is termed "preferential" because the differencing direction in the predictor and corrector steps can be changed at will, provided these changes are consistent with the second order accuracy.

When applied to a system of equations of form:

$$E_x + F_y + G_z = 0 \quad , \quad (7)$$

MacCormack's predictor-corrector is written as:

$$\text{Predictor: } \tilde{E}_{j,k}^{n+1} = E_{j,k}^n - \frac{\Delta x}{\Delta y} (F_{j+1,k}^n - F_{j,k}^n) - \frac{\Delta x}{\Delta z} (G_{j,k+1}^n - G_{j,k}^n) \quad (8)$$

$$\text{Corrector: } E_{j,k}^{n+1} = \frac{1}{2} [E_{j,k}^n + \tilde{E}_{j,k}^{n+1} - \frac{\Delta x}{\Delta y} (\tilde{F}_{j,k}^{n+1} - \tilde{F}_{j-1,k}^{n+1}) - \frac{\Delta x}{\Delta z} (\tilde{G}_{j,k}^{n+1} - \tilde{G}_{j,k-1}^{n+1})]$$

However, as can be seen from Appendix A, the system of equations has the form:

$$E_x + F_y + G_z + H = 0 \quad . \quad (9)$$

To accommodate the nonhomogeneous term, it was necessary to add the quantities:

$$\begin{aligned} \text{Predictor: } & - H_{j,k}^n \Delta x \\ \text{Corrector: } & - \frac{1}{2} \tilde{H}_{j,k}^n \Delta x \end{aligned} \quad (10)$$

to Equations 8.

For two-dimensional flow around circular cones, amplification theory predicts the numerical method is stable, pro-

vided (using present notation):

$$|\sigma_{\max}| \frac{\Delta E}{\Delta \delta} < 1 \quad (11)$$

and

$$|\lambda_{\max}| \frac{\Delta E}{\Delta \beta} < 1 \quad (12)$$

are satisfied simultaneously. Due to the coupled effects in the eigenvalue structure, the satisfaction of Equation 11 was tantamount to the satisfaction of Equation 12.

The eigenvalues, σ and λ , are as derived in Appendix D, and σ_{\max} was located at the outermost mesh point of the windward side of a body at angle of attack. This causes the flow on the windward side of the body to be integrated optimally while the leeward side is integrated in less than optimal fashion. For this problem it was found that:

$$|\sigma_{\max}| \frac{\Delta E}{\Delta \delta} < 1.20 \quad (13)$$

is violated at the solution. This is due to the fact that approximation error theory is based on linear Fourier analysis and the present problem is nonlinear.

It was also found that choosing initial conditions at some point E , integrating to some point $E + \Delta E$, and then choosing new initial conditions as initial conditions for another integration step at point E , enhanced stability and

numerical accuracy. In effect, the numerical method was continuously operating at (or near) the optimum mesh ratio.

As can be seen from Appendix D:

$$|\sigma_{\max}|, |\lambda_{\max}| \propto \frac{1}{\xi} \quad (14)$$

so that after a number of downstream integrations, the numerical method would no longer be functioning optimally.

Initial Conditions

Initial conditions for the flow variables can be chosen in at least two ways. First, the shock shape and position, and values of flow variables between the shock and the body can be approximated. This method is quite efficient with regard to computer effort, if the approximations are reasonable. Moretti (21) indicates that the choice of initial data does not affect the end results. Secondly, the individual flow variables can be initialized to freestream values. Although quite inefficient, this method was chosen since it resembles impulsively starting the body. Even though the transient, numerical values for the flow variables between the shock and body surface may not coincide with the true, physical solution, the shock build-up can still be witnessed. Appendix E shows how the freestream quantities were derived.

Boundary Conditions

From analytical considerations, the exact boundary condition applied to the surface of the body is:

$$\vec{q} \cdot \nabla F(\xi, \delta, \beta) = 0 \quad , \quad (15)$$

where $F(\xi, \delta, \beta) = 0$ is the equation of the body. Also, across the shock surface, the Rankine-Hugoniot equations must be satisfied. However, numerical methods cannot use these equations directly. This is especially true of finite difference methods, due to their differencing nature. Therefore, equivalent numerical boundary conditions were derived and applied at the body and shock.

The reflection boundary condition used in this study (see Appendix B), assumed even functions of pressure, density, and tangential velocity and an odd function of normal velocity across the body surface. This gave the necessary sublayer data points, as a function of the known superlayer points, required by the MacCormack predictor step. Since elliptic cones have a plane of flow symmetry about the $\beta = 0^\circ$, 180° meridian (see Figure 1), numerical integration was carried out over one half the conical surface. This plane of symmetry forms another boundary across which pressure, densi-

ty, u-velocity, and v-velocity were assumed to be even functions and w-velocity was assumed to be an odd function.

The mesh in the direction outward from the body, in the direction of increasing δ , extended far enough to overlap the estimated shock position. In this manner, the shock could, at best, be captured between two mesh points. Pressure, density and velocity outside the shock were assumed to have freestream values.

Due to first order numerical accuracy in the MacCormack predictor, the velocity vector, \vec{q}_1 , was not, in general, tangent to the body surface as dictated by Equation 15. The entropy boundary condition (see Appendix C) used by Abbett (1) accounted for this misalignment and "brought" the velocity vector back to tangency by utilizing a local compression or expansion through an angle $\Delta\theta$. With $\Delta\theta$ known, the pressure, P_2 , following the expansion or compression was calculated; and with pressure known, density, ρ_2 , at the body was obtained by utilizing the perfect gas equation of state. From energy considerations, the velocity magnitude, $|\vec{q}_2|$, was found. Finally, from vector relations inherent in the flow geometry, the direction of the resultant velocity, \vec{q}_2 , was obtained. A complete derivation is presented in Appendix C.

For this problem, it was necessary to apply the entropy boundary condition after the predictor step. No analytical proof for this conclusion is readily available. However, it

is believed that the immediate application of the entropy boundary condition (i.e., after the predictor) allows the corrected surface boundary conditions to be propagated into the flow field sooner, resulting in better numerical behavior. In this study, application of the boundary condition after the corrector resulted in instability, since a continual expansion was eventually attained, which drove the body surface pressure to zero.

The boundary conditions for the elliptic cone were derived in the physical Cartesian system and transformed to the computational polar system. This resulted in the application of the elliptic boundary conditions to a circular cone. Since the numerical method discretized the body, the method could deduce the body geometry only through the boundary condition relations.

Method of Solution

The coordinate system presented was selected primarily because it yielded a circular cone in the computational system. The significance of this, apart from the previously mentioned inversion simplifications, was that boundary conditions could be applied to a constant coordinate surface (e.g., constant circular cone angle, δ).

The desired elliptic body shape could be acquired by choosing appropriate values for the semimajor and semiminor axes, a and b , and the characteristic length in the body axis direction c , which governed the slenderness of the configuration. After transforming the elliptic body to the computational polar system, the number of angular increments around the conical body (NBETA) were chosen, and the outermost shock position (SHOCK) was estimated. These choices defined the mesh increments, $\Delta\beta$ and $\Delta\delta$, used in the numerical integration, as follows:

$$\Delta\beta = \frac{1900}{\text{NBETA}}$$

(16)

$$\Delta\delta = \frac{(\text{SHOCK} - \text{Cone Semiapex Angle})}{\text{NDELTA}} .$$

Integration was performed from $\beta = 0^\circ$ to $\beta = 180^\circ$ in the positive sense of trigonometry (see Figure 1). As indicated before, the $\beta = 0^\circ, 180^\circ$ meridian is the plane of flow symmetry and therefore reflection across this plane was used. This reflection compensated for the backward and forward differencing requirements of the MacCormack predictor-corrector sequence.

For the reflection boundary condition, the predictor and corrector steps were completed before the boundary condition was applied. This approach demonstrated good stability char-

acteristics and yielded satisfactory solutions. As previously noted, the entropy boundary condition was applied after the predictor step.

Program execution was terminated automatically when the convergence criterion was met. This criterion was defined as:

$$\left| \frac{p^n}{p^{n-1}} - 1 \right| < \epsilon \quad (17)$$

where p^n is the present pressure, p^{n-1} is the pressure of the previous iteration, and ϵ is the convergence tolerance (usually $\epsilon = 0.001$). Equation 17 was satisfied for ten consecutive iterations before the execution was terminated. This gave rise to a conservative deviation of 0.1% per iteration.

The program logic and underlying theory were first tested by investigating circular cones at zero and small indices. Agreement with other accepted solutions (e.g., Babenko, et al. (4)) was such that the approach was deemed valid, and the elliptic cone problem was then confronted. Results of the conical computations are reported in the next section and the elliptic cones are treated in the sections following.

THE CIRCULAR CONE

In order to test the viability of the approach in the previous section, the reflection and entropy boundary conditions were applied to a $\delta = 10^\circ$ pointed, circular cone at $M_\infty = 5.0$ and angles of attack of $\alpha = 0^\circ$ and 5° . This circular configuration was selected for a number of reasons. First, in the past two decades there have been many circular cone studies, so that much comparison data were available. Second, the conical flow assumptions made concerning the flow field around the elliptic cone were also valid for the circular cone. Thus, the same approach could be used for both problems. Third, having a constant coordinate surface, the circular cone was mathematically simple to describe and an easy body to which boundary conditions could be applied. Finally, some measure of merit was necessary to judge the quality of the reflection and entropy boundary conditions. The circular cone, with its plethora of comparison material, satisfied these necessities.

The initial concern was for the numerical location of the shock. Due to the finite difference mesh, the shock could, at best, be captured between two mesh points. Because of this, the step discontinuity in the derivatives of flow variables across the shock could not be represented exactly by the numerical method. Therefore, there was some doubt as

to whether the shock position could be accurately depicted. However, as seen from Figures 2, 3, 4 and 5, the shock position is clearly defined and reasonably accurate. Figure 6 shows the numerical shock position overlying Babenko's (4) comparison data. The shock positions calculated by each boundary condition were quite close and are represented by the same data point in the figure. As can easily be seen, the numerical shock position representation is quite good. For the $\alpha = 0^\circ$ case, the angular shock position, from NACA R-1135 (14), is $\delta = 15.7^\circ$, while the numerical angular shock position was calculated to be $\delta = 15.5^\circ$.

For the circular cone at zero angle of attack, the entropy boundary condition invariably yielded a better representation of the pressure and density variation outward from the body. Figures 2 and 3 show that the entropy boundary condition yielded pressure and density solutions that match those of Babenko, while the reflection boundary condition yielded solutions that were 1.5% to 2.0% high. Although obviously not as accurate as the entropy boundary condition, especially at the body surface, the reflection boundary condition should not be completely discounted. Due to slow convergence properties of the reflection boundary condition, and a premium on computer time, the numerical integration was terminated before convergence. However, as integration continued, the reflection boundary condition solutions ap-

proached those obtained by Babenko.

For the circular cone at angle of attack ($\alpha = 5^\circ$), these same trends were witnessed. The conical body at incidence gave rise to pressure and density gradients around the body. This effect can be seen in Figures 4 and 5, where pressure and density are plotted for three angular positions ($\beta = 0^\circ, 90^\circ$ and 180°) around the body. The windward side ($\beta = 180^\circ$), the region of greatest compression, is aptly depicted by the outward pressure variations from the body to the crisp numerical shock. The leeward side of the body ($\beta = 0^\circ$), the region of least compression, shows a somewhat poorer pressure and shock representation. This is due to the eigenvalue structure and its previously noted effects on the numerical integration around the body.

Of greatest concern were the density anomalies at the body surface, seen in Figures 3 and 5. This misbehavior resulted from the assumptions made regarding the the flow near the body and the subsequent reflection boundary condition. To eliminate this problem, the entropy boundary condition was applied after the numerical process had been brought to near convergence using the reflection boundary condition. This led to the most dramatic evidence of the beneficial traits of the entropy boundary condition. Figure 7 shows the effect of the entropy boundary condition. For the $\alpha = 0^\circ$ case, the reflection density solution at the body was low by 26%, but

when the entropy boundary condition was used, the body value of density coincided with Babenko's results. This same behavior can be witnessed for the $\alpha = 5^\circ$ case, although agreement at the body is not exact.

It was found that for configurations having gradients of flow variables in the lateral direction (the β -direction), the numerical solution demonstrated a "lag" when the entropy boundary condition was applied. After only a few integrations (1 or 2) utilizing the entropy condition, solutions on the body were very close to the comparison data. However, as integration continued, further convergence was painfully slow.

The introduction of the entropy boundary condition did not affect the body pressure as much as it did the body density, since the reflection boundary condition yielded good representative pressure values. From Figure 8, for the $\alpha = 0^\circ$ situation, the entropy boundary condition again brought the surface pressure solution into accordance with the comparison pressure solution. For the $\alpha = 5^\circ$ case, the characteristic lag was again encountered.

These preliminary results led to the conclusion that the entropy boundary condition better represented the actual flow field for the circular cone. Therefore, due to the aforementioned similarities between the elliptic and circular cone problems, it was concluded that the entropy boundary condi-

tion would yield the better representation of the flow around the elliptic cone. With this deduction, the plan of attack on the elliptic cone was formulated.

The geometry and orientation of the configuration would be defined, and numerical integration, using the reflection boundary condition, would be used to acquire a nearly converged solution. This solution would then be compared to existing data and, if deemed satisfactory, would be used as initial conditions for further numerical integration, incorporating the entropy boundary condition. This integration would be continued until convergence (or near convergence) was attained.

THE ELLIPTIC CONE

Introduction

A major problem in studying the supersonic flow about elliptic cones is the meager supply of accessible elliptic cone comparison data. Both analytic data and sufficient experimental information are difficult to acquire. However, with the available literature and consideration of the elliptic-circular cone similarities, a "thumbnail sketch" of the elliptic cone problem can be divined.

Melnick (18) indicates the presence of vortical singularities in the semiminor axis plane, at the surface of an elliptic cone at incidence. According to Melnick, these vortical singularities, arising from the inviscid flow assumptions, are the terminal points of the cross flow streamlines. Melnick then concludes that "entropy, density and radial velocity are generally multivalued at these points." Moretti (20) states that the absence of viscous effects not only limits the validity of the solution, but also requires the angle of attack to be less than the conical semiapex angle, if a leeward shock is to be observed. In Sears (22), Ferri calls attention to the possible lift-off of the leeward vortical singularity as angle of attack is increased. Since the angle of attack was kept small, the vortical lift-off was not

witnessed.

For the elliptic cone at zero incidence, the stagnation streamline passes through the shock and impinges on the elliptic cone in the $\beta = 90^\circ$ plane. Thus, the entire elliptic surface, with the possible exception of the vortical singularities, is an isentropic stream surface. Since the location of the streamline impingement is known for the zero incidence case, numerical calculation of the body entropy is facilitated. However, for the angle-of-attack case, the stagnation streamline strikes the elliptic body somewhere between $\beta = 90^\circ$ and 180° , depending on the flow velocity and the angle of attack. The exact location of the impingement is pin-pointed where the cross flow velocity is zero.

To find the entropy on the body, the entropy of the stagnation streamline must be calculated. But since the numerical technique discretizes the flow field, the stagnation streamline away from the body can only be approximated by some interpolation method. This may lead to moderate errors in surface entropy values and is a source of further study.

Another origin of problems is the area near the $\beta = 90^\circ$ plane. In this region, the large gradients of the flow variables are difficult to calculate precisely, due to the discretization of the flow field. This behavior could, quite possibly, give rise to the characteristic "lag" noted for the circular cone solutions and accentuated in the elliptic cone

solutions. A more accurate description of the flow field in the $\beta = 90^\circ$ region could be acquired by further clustering of data points in this area.

In order to facilitate the comparison with Chapkis' (7) results, the following parameters were chosen for the elliptic cone at zero incidence: $a/b = 2$, $c = 5.6667$ and $M_\infty = 5$. For the elliptic cone at angle of attack, comparison with Martellucci's (17) theory required an elliptic cone with different defining parameters. These parameters were defined as follows: $a/b = 1.788$, $c = 1.0$ and $M_\infty = 3.09$.

Zero Angle of Attack

As in the circular cone study, first consideration was given to the shock position around the body. However, due to the lack of analytical corroborative material, some amount of intuition must be used in judging the numerical results. Chapkis (7) indicates that the shock should be closer to the body in the semimajor axis plane than it is in the semiminor axis plane. This is due to the high pressure region near the elliptic "shoulder" (i.e., near the $\beta = 90^\circ$ plane) and to the resulting pressure gradient from the shoulder toward the $\beta = 0^\circ$ and 180° planes. This observation is verified in Figure 9. The shock positions calculated by each boundary condition were essentially coincident. Maximum pressure was

observed at the stagnation streamline, located on the $\beta = 90^\circ$ plane, which indicated the presence of a strong shock. As mentioned before, the entropy value required by the entropy boundary condition was calculated using flow variables acquired from this plane.

The variation of surface pressure coefficient around the elliptic body is presented in Figure 10. The reflection boundary condition matches well Chapkis' (7) theoretical data, except in the range $80^\circ \leq \beta \leq 100^\circ$, which roughly coincides with the region of greatest body curvature. The solution obtained using the entropy boundary condition, also shown in Figure 10, is far from the theoretical expectations. The figure indicates a more constant surface pressure coefficient for $0^\circ < \beta < 90^\circ$, while the $70^\circ \leq \beta < 90^\circ$ region demonstrates a sharper surface pressure coefficient gradient. A weak local expansion in this latter region would explain this behavior, although this is pure conjecture. (This will be discussed in greater detail in the following section.) Due to the symmetry of the flow, the region $90^\circ \leq \beta \leq 180^\circ$ should match the $0^\circ \leq \beta \leq 90^\circ$ region. However, Figure 10 shows an anomaly near $\beta = 115^\circ$ for both boundary conditions. At this point, either numerical "overshoot" or eigenvalue problems is suspected. Due to lack of computer funding and time, a more thorough analysis could not be carried out.

Angle of Attack

For the angle-of-attack case, the shock position around the body was again investigated. The results are presented in Figure 9. The point at which the shock most closely approaches the body indicates the strong portion of the shock and the approximate location of the stagnation streamline. As the angle of attack was increased, the stagnation streamline moved in the direction of increasing β . For $\alpha = 5^\circ$, the location of the stagnation point on the body was $\beta \approx 98^\circ$. The uncertainty about the lateral stagnation point, and the extension of the stagnation streamline into the flow field, were major sources of difficulty in the application of the entropy boundary condition. Without a reasonably accurate approximation of the stagnation streamline position, entropy on the body surface could not be accurately calculated. Therefore, the boundary condition was less reliable.

Figure 11 shows the variation of surface pressure coefficient, calculated from each boundary condition, around the body, compared to Martellucci's (18) theoretical data. Generally speaking, agreement is good; however, the $50^\circ \leq \beta < 80^\circ$ region is one notable exception.

It seems intuitive that supersonic flow around a corner (such as the flow from the stagnation point around the el-

liptic shoulder) would experience a slight, but noticeable, expansion. No theoretical evidence of this was found in the literature available; however, experiments conducted by Zakay and Visich (26) for a similar elliptic cone subjected to similar flow conditions, but at $\alpha = 15^\circ$, seem to verify this conjecture.

Figure 11 appears to indicate a locally expanded flow for both boundary conditions in the previously noted $50^\circ \leq \beta \leq 80^\circ$ region, although the entropy boundary condition yields a more pronounced behavior. In Figure 12, the density around the body is plotted, showing the entropy and reflection boundary condition behavior. No comparison data was available, but the behavior seems to lend credence to the "expansion hypothesis."

The validity of the underlying theory and assumptions, and the applicability of the entropy boundary condition for more closely approximating surface flow characteristics, have been demonstrated. More thorough investigation of the numerical behavior of the entropy boundary condition and a more concise method for obtaining the surface entropy are needed.

ACKNOWLEDGEMENTS

The author wishes to express his appreciation to Dr. Dale Anderson for his guidance throughout the course of this study and to the Iowa State University Engineering Research Institute and Department of Aerospace Engineering for financial support. The author also wishes to convey a special thanks to his wife, Connie, for her patience throughout the period of his graduate education. Without her encouragement and dauntless optimism, this graduate degree would have been most difficult to obtain.

BIBLIOGRAPHY

1. Abbett, M., Quarterly Report, Aerotherm Project 6147, Aug. 1971.
2. Anderson, D. A. and Vogel, J. M., "Numerical Solutions of Flowfields Behind Rectangular Wings," Engineering Research Institute, Iowa State University, Ames, Iowa, July 1971.
3. Anderson D. A. and Vogel, J. M., "Numerical Calculations of Flowfields," Quarterly Report, Engineering Research Institute, Iowa State University, Ames, Iowa, July-Aug. 1971.
4. Babenko, V. I., Voskresenskiy, G. B., Lyubimov, A. N. and Pusanov, V. V., "Three Dimensional Flow of Ideal Gas Past Smooth Bodies," NASA TT F-380, Apr. 1966.
5. Briggs, R. R., "The Numerical Calculation of Flow Past Conical Bodies Supporting Elliptic Conical Shock Waves at Finite Angles of Incidence," NASA TN D-340, Nov. 1960.
6. Brook, J. W., "The Calculation of Nonlinear Supersonic Conical Flows by the Method of Integral Relations," Flight Dynamics Research and Technology Division Report 64-7, July 1964.
7. Chapkis, R. L., "Hypersonic Flow over an Elliptic Cone: Theory and Experiment," Journal of the Aerospace Sciences, Vol. 28, No. 11, Aug. 1953, pp. 844-854.
8. Ferri, A., "Supersonic Flow Around Circular Cones at Angles of Attack," NACA TN-2236, Nov. 1950.
9. Ferri, A., "The Linearized Characteristics Method and its Application to Practical Nonlinear Supersonic Problems," NACA TN-2515, Oct. 1951.
10. Ferri, A., Ness, K. and Kaplita T. T., "Supersonic Flow over Conical Bodies without Axial Symmetry," Journal of the Aerospace Sciences, Vol. 20, No. 8, Aug. 1953, pp. 563-571.
11. Ford, R. A., "An Approximate Solution for Axially Symmetric Flow over a Cone with an Attached Shock Wave," NACA TN-3485, Oct. 1955.

12. Jones, D. J., "Numerical Solutions of the Flow Field for Conical Bodies in a Supersonic Stream," National Aeronautical Establishment, Ottawa, Canada, Aeronautical Report LP-507, (NRC No. 10361), July 1968.
13. Kahane, A. and Solarski, A., "Supersonic Flow About Slender Bodies of Elliptic Cross Section," Journal of the Aerospace Sciences, Vol. 20, No. 8, Aug. 1953, pp. 513-524.
14. Kutler, P., "Application of Selected Finite Difference Techniques to the Solution of Conical Flow Problems," Unpublished Ph.D. Thesis, Iowa State University, Ames, Iowa, Oct. 1969.
15. Laboratory Research Staff, Ames Research Center, Moffett Field, California, "Equations, Tables, and Charts for Compressible Flow," NACA R-1135, 1953.
16. Lomax, H., Kutler, P. and Fuller, F., "The Numerical Solution of Partial Differential Equations Governing Convection," Ames Research Center, Moffett Field, California, 1969.
17. McCormack, R. W., "The Effect of Viscosity in Hypervelocity Impact Cratering," AIAA Paper No. 65-354, 1969, pp. 1-7.
18. Martellucci, A., "An Extension of the Linearized Characteristics Method for Calculating the Supersonic Flow Around Elliptic Cones," Journal of the Aerospace Sciences, Vol. 27, No. 9, Sept. 1960, pp. 667-674.
19. Melnick, R. E., "Vortical Singularities in Conical Flow," AIAA Journal, Vol. 5, No. 4, Apr. 1967, pp. 631-637.
20. Moore, F. K., "Three-Dimensional Boundary Layer Flow," Journal of the Aerospace Sciences, Vol. 20, No. 8, Aug. 1953, pp. 525-534.
21. Moretti, G., "Inviscid Flow Field About a Pointed Cone at an Angle of Attack," AIAA Journal, Vol. 5, No. 4, Apr. 1967, pp. 789-791.
22. Rakich, J. V., "Application of the Method of Characteristics to Noncircular Bodies at Angle of Attack," 67-228, Oct. 1967, Ames Research Center, Moffett Field, California.

23. Sears, W. B., ed., General Theory of High Speed Aerodynamics, 1st ed., Vol. 6, Princeton University Press, Princeton, New Jersey, 1965, pp. 721-746.
24. South, J. C. and Klunker, E. B., "Methods for Calculating Nonlinear Conical Flows," SP-228, Oct. 1969, Ames Research Center, Moffett Field, California.
25. Van Dyke, M. D., "The Elliptic Cone as a Model for Non-linear Supersonic Flow Theory," Journal of Fluid Mechanics, Vol. 1, No. 1, 1956, pp. 1-15.
26. Ward, G. N., "Supersonic Flows Past Slender Pointed Bodies," Quarterly Journal of Mechanics and Applied Mathematics, Vol. 2, 1949, pp. 74-97.
27. Zakkay, V. and Visich, M., Jr., "Experimental Pressure Distributions on Conical Elliptical Bodies at $M_\infty = 3.09$ and 6.0," Polytechnic Institute of Brooklyn, PIBAL Report No. 467, Mar. 1959.

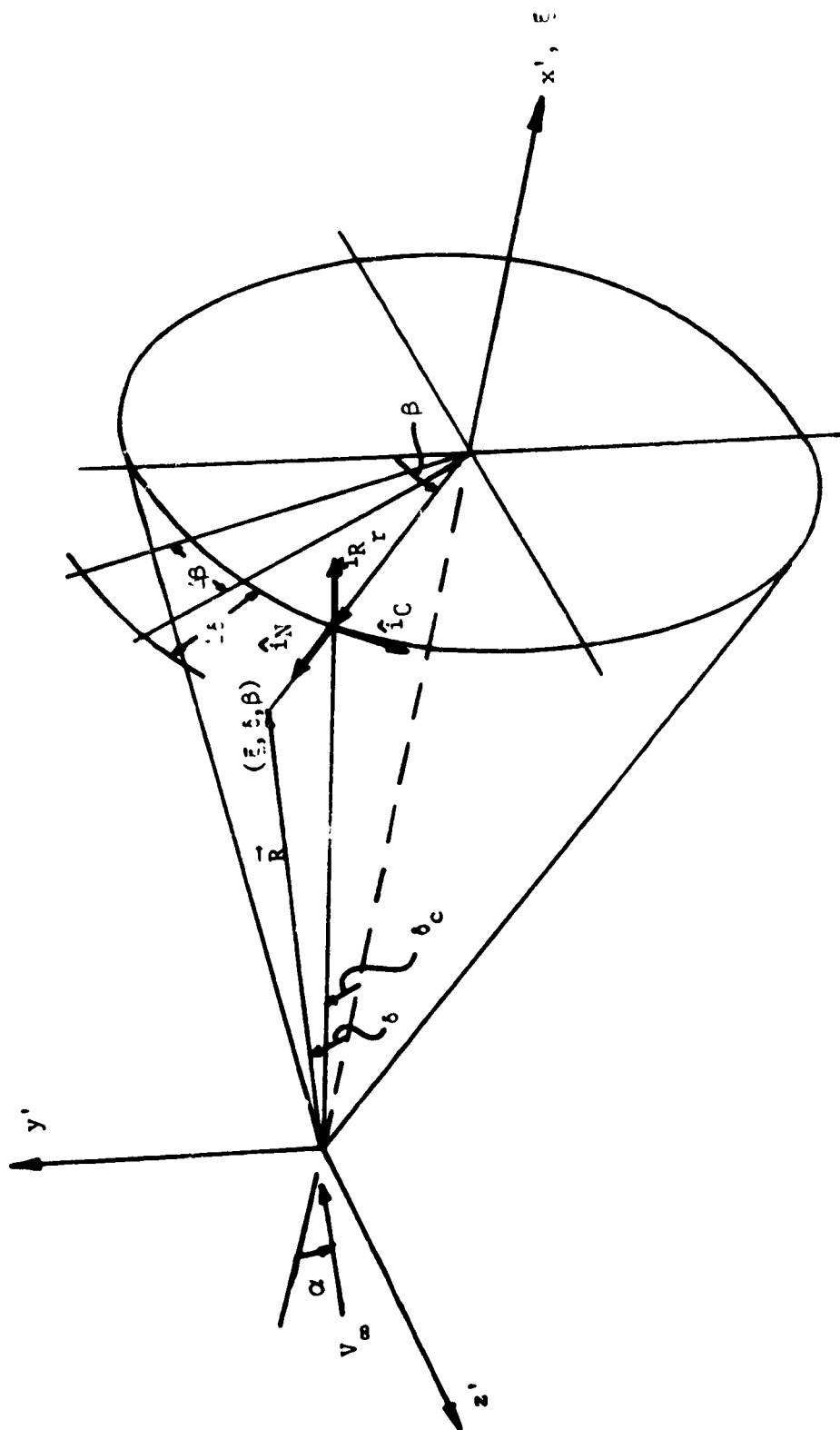


Figure 1 Computational Cartesian and polar coordinate systems

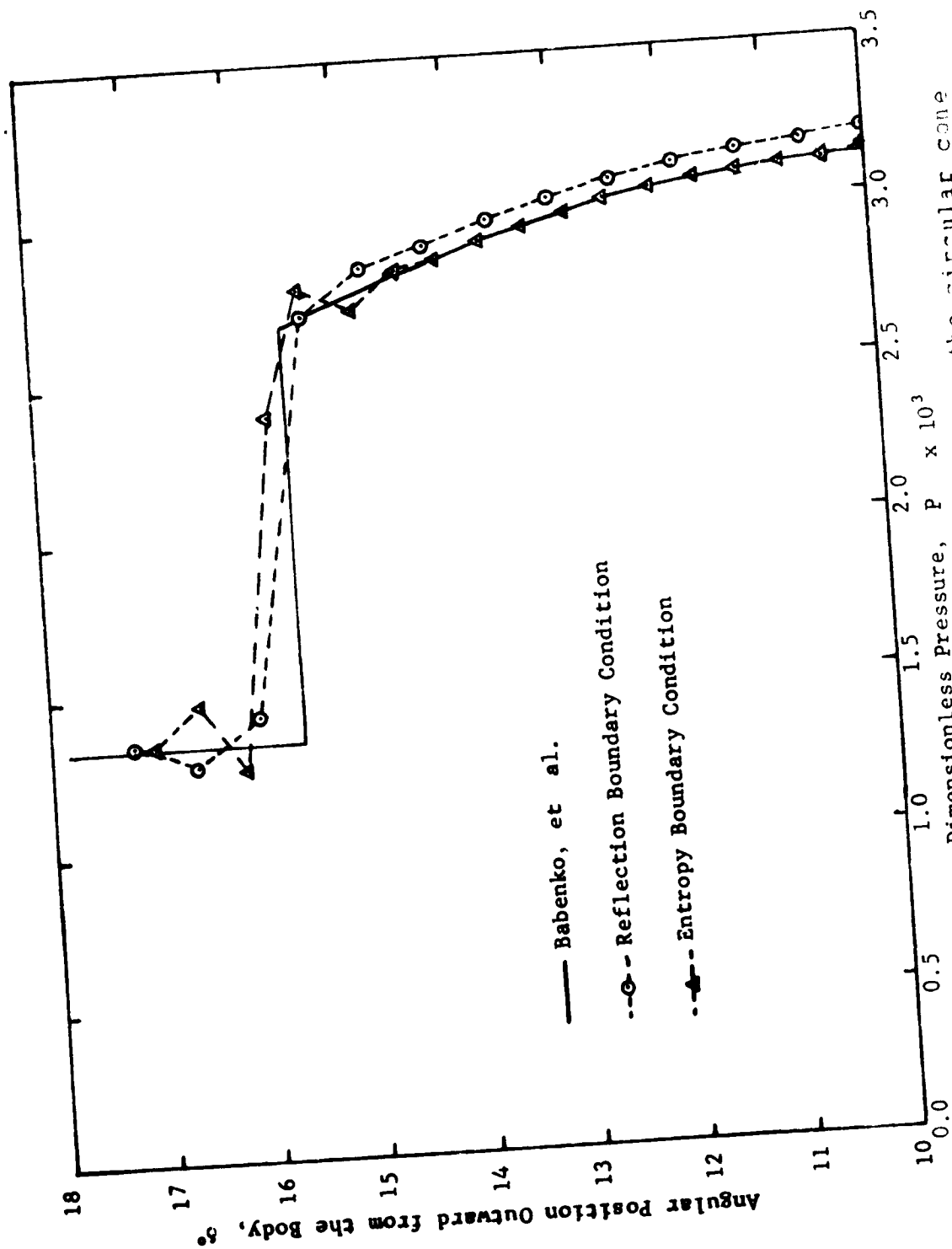


Figure 2 Dimensionless pressure normal to the circular cone at $\alpha = 0^\circ$

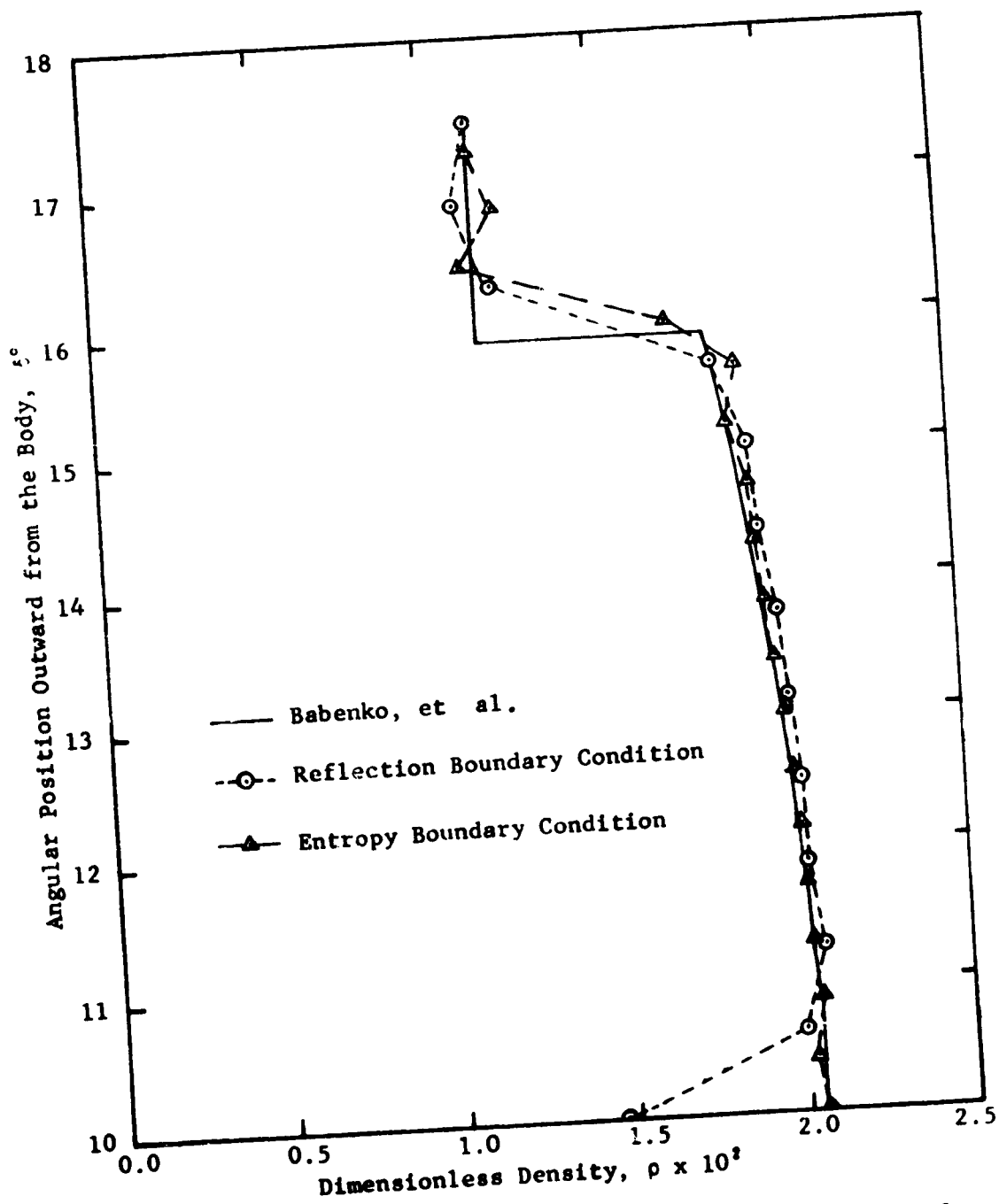


Figure 3 Dimensionless density normal to the circular cone at $\alpha = 0^\circ$

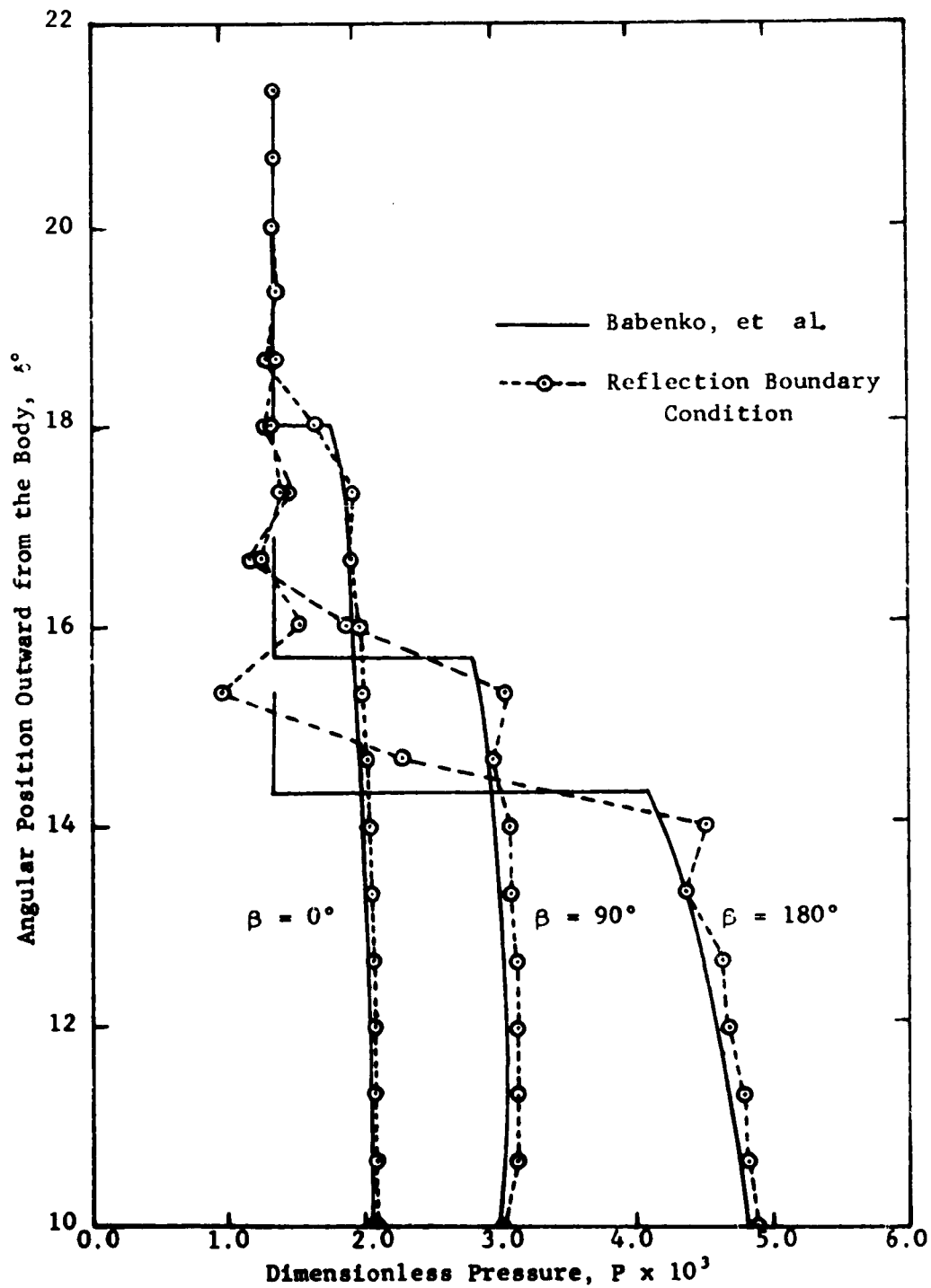


Figure 4 Dimensionless pressure normal to the circular cone at $\alpha = 5^\circ$

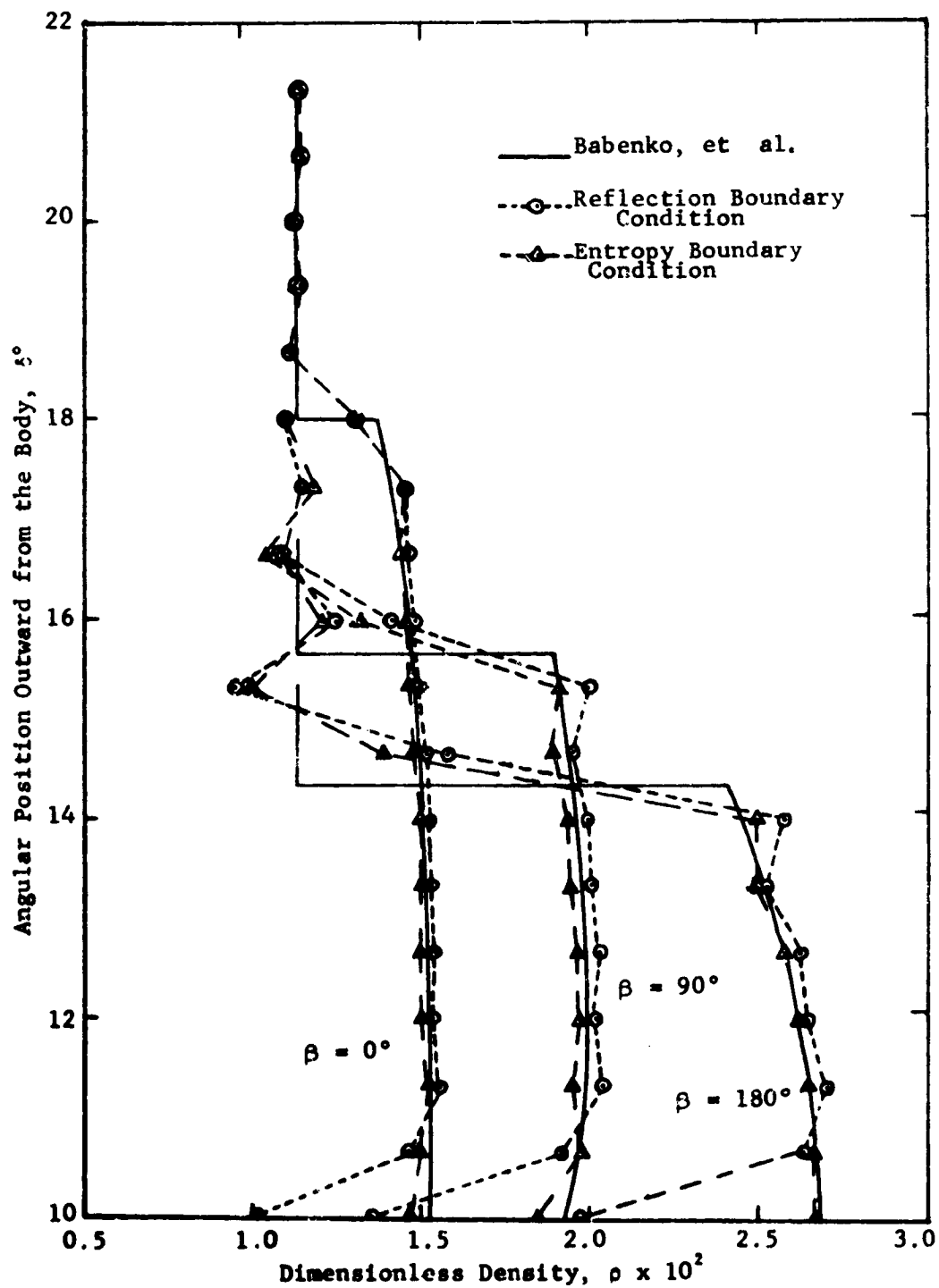


Figure 5 Dimensionless density normal to the circular cone at $\alpha = 5^\circ$

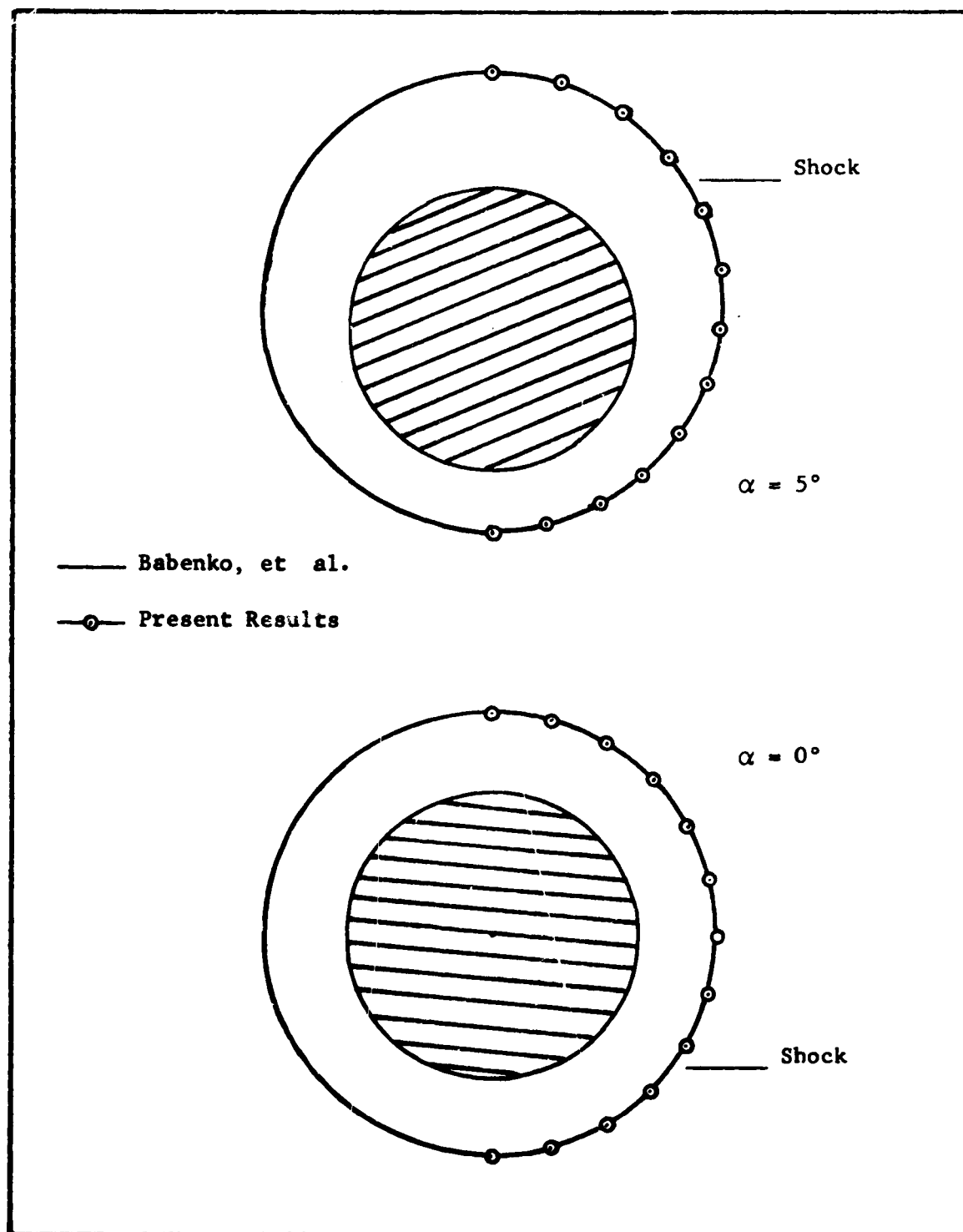


Figure 6 Shock position around the circular cone at $\alpha = 0^\circ$ and 5°

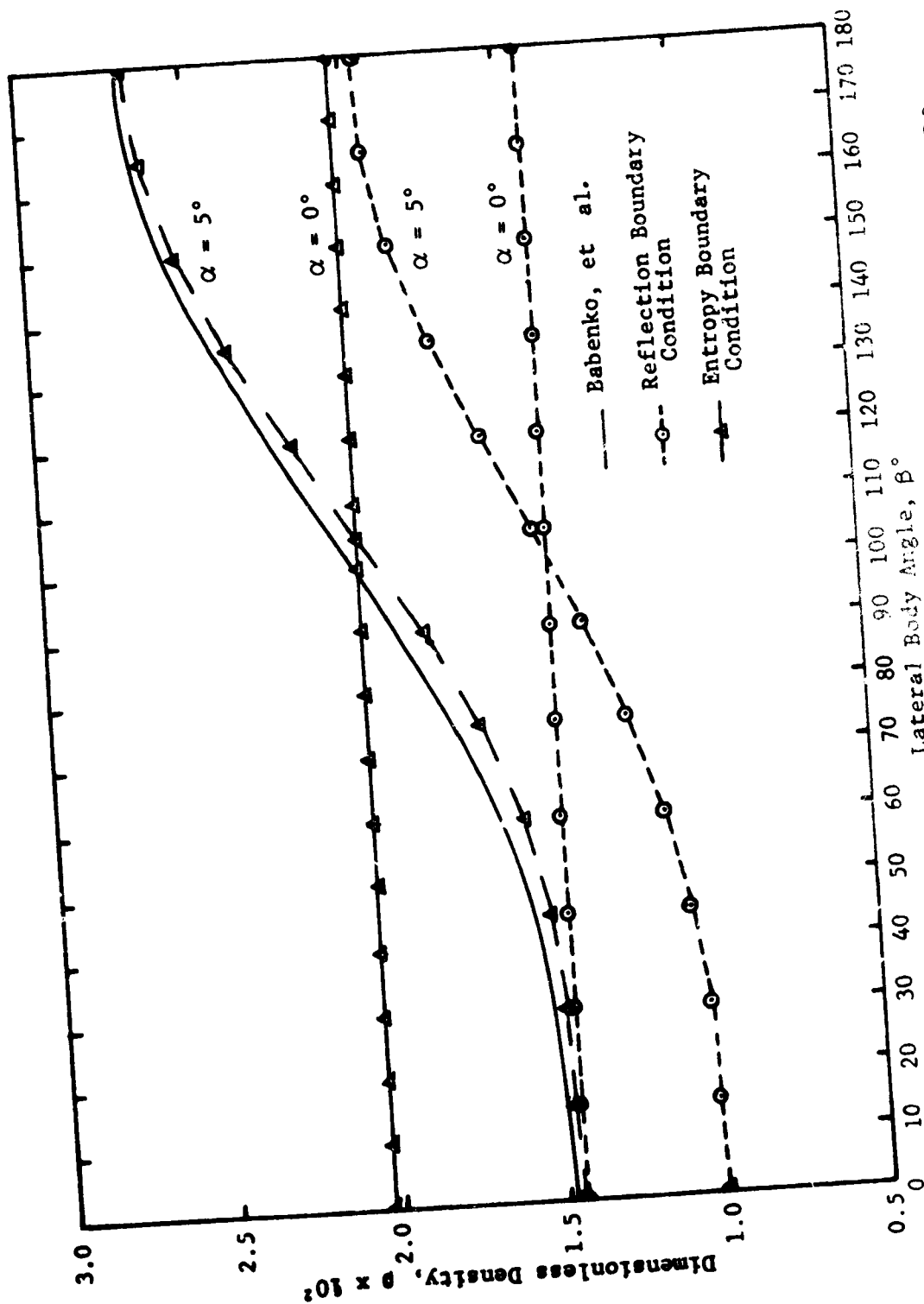


Figure 7 Lateral density distribution for a circular cone

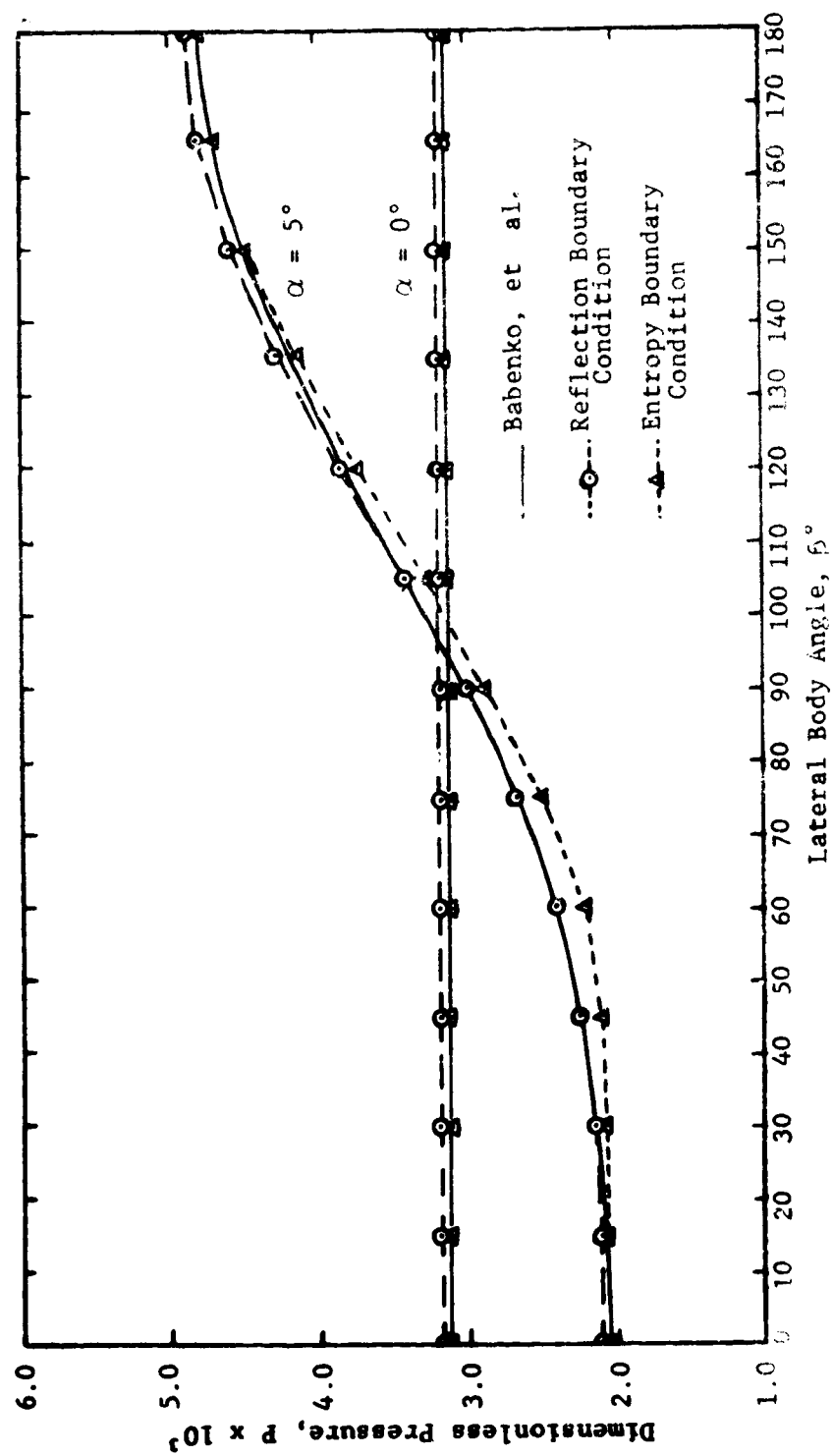


Figure 3 Lateral pressure distribution for the circular cone

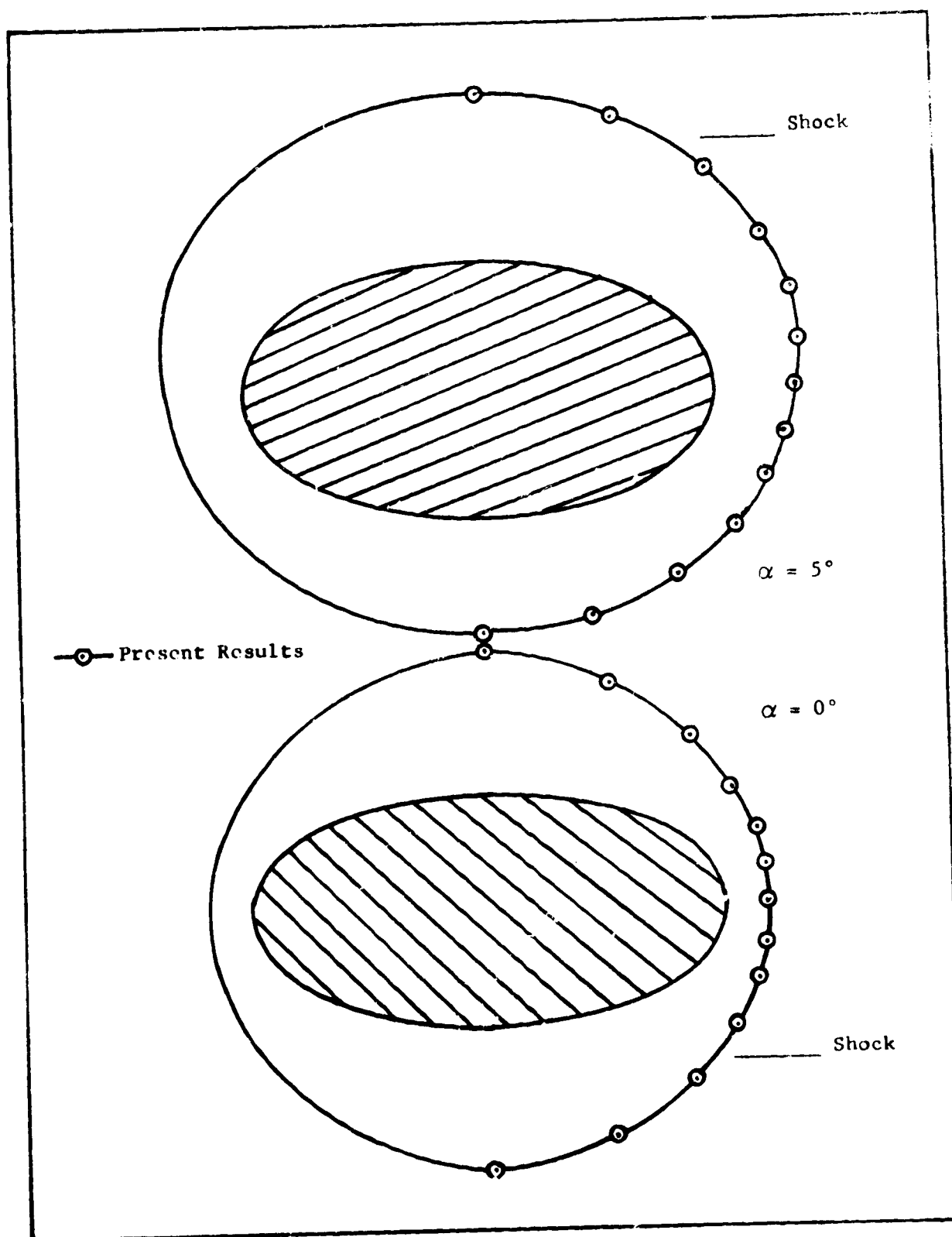


Figure 9 Shock position around the elliptic cone at $\alpha = 0^\circ$ and 5°

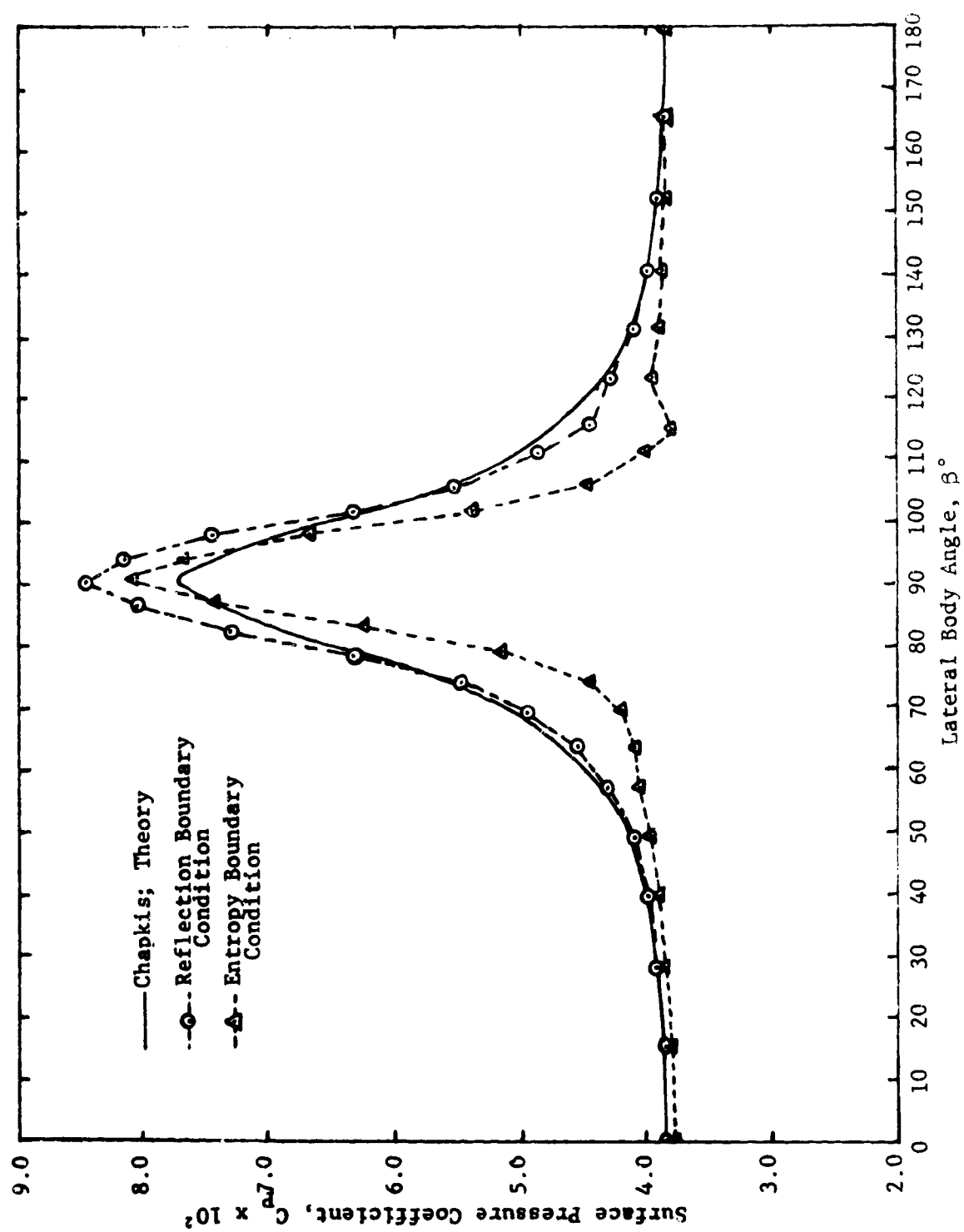


Figure 10 Lateral pressure distribution for the elliptic cone at $\alpha = 0^\circ$

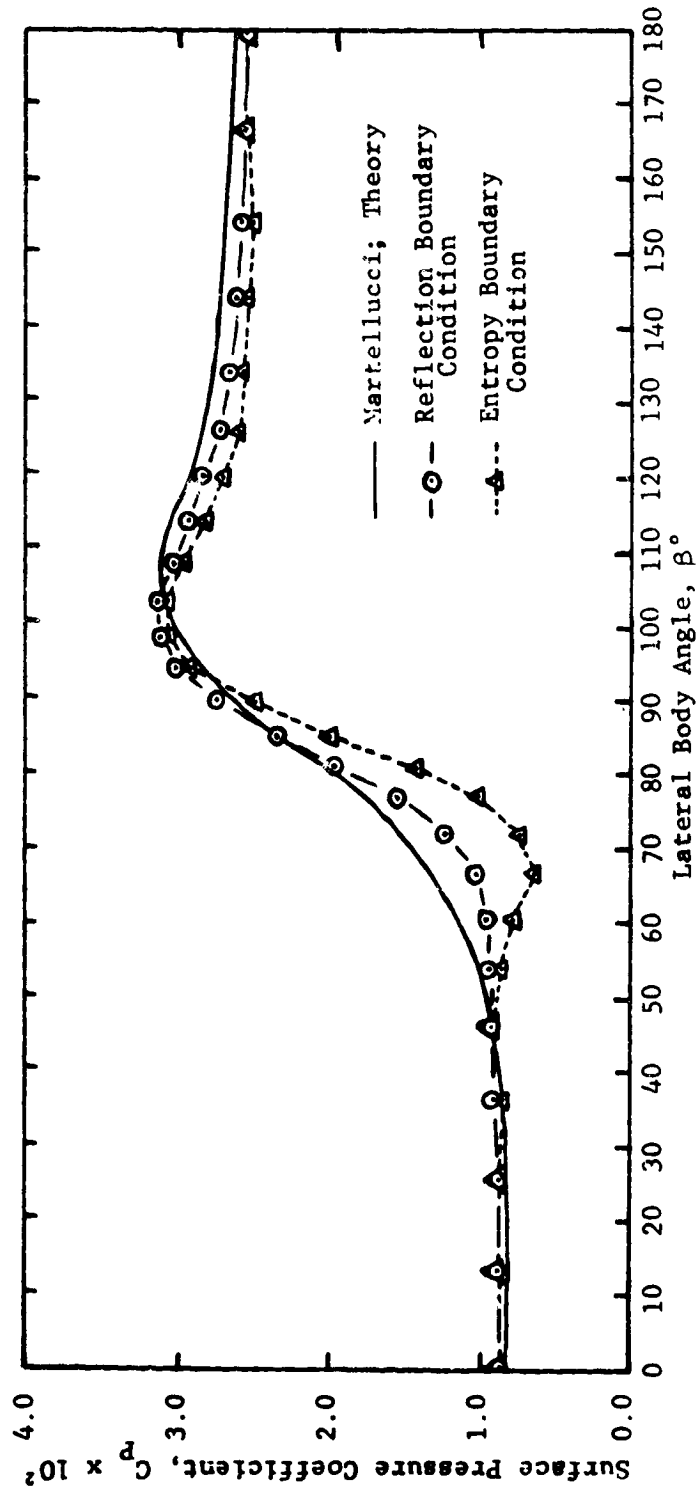


Figure 11 Lateral pressure distribution for the elliptic cone
at $\alpha = 50^\circ$

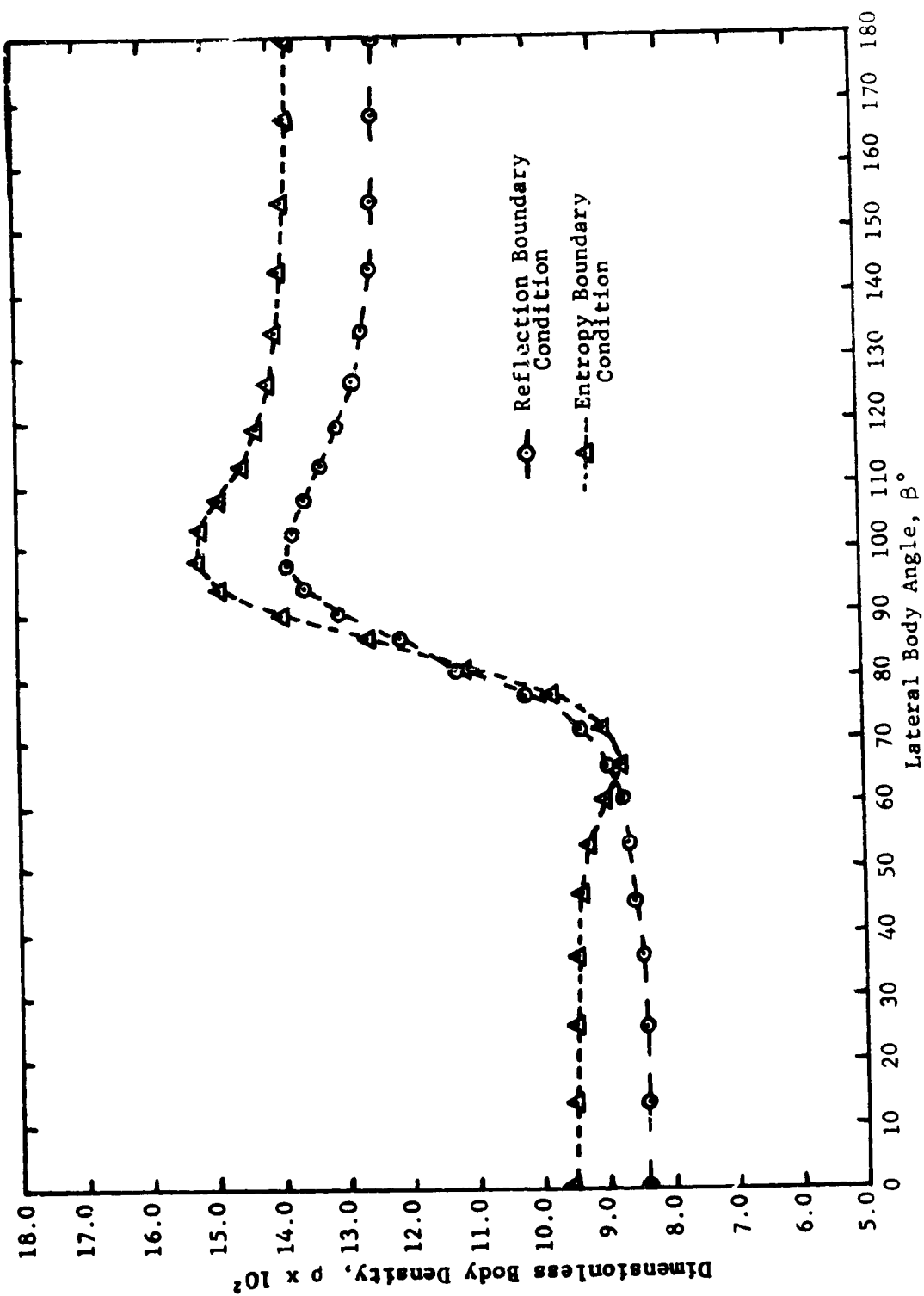


Figure 12 Lateral density distribution for the elliptic cone at $\alpha = 5^\circ$

APPENDIX A: COORDINATE SYSTEM AND CONSERVATIVE EQUATIONS

Coordinate System

The coordinate system chosen, Figure 1, required two transformations to acquire the final computational system. The first transformation was from the Cartesian system, (x, y, z) , to the computational Cartesian system, (x', y', z') , via the transformation:

$$\begin{aligned} x' &= x \\ y' &= ay \\ z' &= bz \end{aligned} \quad , \quad (A-1)$$

where a and b are the semimajor and semiminor axes of the elliptic cross section, respectively.

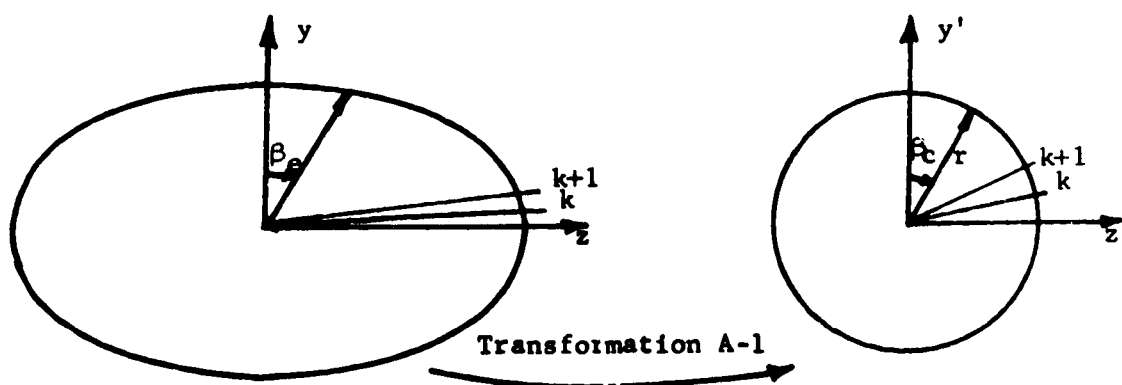


Figure A-1 Coordinate system transformation

The effect of the transformation provided by Equations A-1 is the deformation of the elliptic cross sections in the Cartesian plane into circular cross sections in the computational plane, see Figure A-1.

The general equation for a right elliptic cone is:

$$\left(\frac{Y}{b}\right)^2 + \left(\frac{Z}{a}\right)^2 = \left(\frac{X}{c}\right)^2 \quad (A-2)$$

Referring to Figure A-1 and Equations A-1, it can be seen that Equation A-2 can be written as:

$$(y')^2 + (z')^2 = \left(\frac{abx'}{c}\right)^2 = r^2 \quad (A-3)$$

The final transformation takes the computational Cartesian system into the computational polar system, (ξ, δ, β) , by utilizing the geometric relationships in Figure 1:

$$\xi = x' = x \quad (A-4)$$

$$\delta = \tan^{-1} \left[\frac{[(y')^2 + (z')^2]^{\frac{1}{2}}}{x'} \right] \quad (A-5)$$

$$\beta = \tan^{-1} \left[\frac{z'}{y'} \right] \quad (A-6)$$

Conservative Equations

The MacCormack second order preferential predictor-corrector requires that the equations of fluid flow, Equations D-6, D-7, D-8, D-9 and D-10, be written in conservation-law form. These fluid flow equations can be written in matrix form and represented by:

$$E_x + F_y + G_z = 0 \Rightarrow E_x + aF_y + bG_z = 0 \quad (A-7)$$

The desired form is:

$$E_\xi + aF_\delta + bG_\beta + H = 0 \quad (A-8)$$

From the chain rule and algebraic manipulations, Equation A-8 becomes:

$$E_\xi - \left(\frac{1}{\xi} \cos \delta \sin \delta\right) E_\delta + a \left[\left(\frac{1}{\xi} \cos^2 \delta \cos \beta\right) F_\delta - \left(\frac{1}{\xi} \cot \delta \sin \beta\right) F_\beta \right] \\ + b \left[\frac{1}{\xi} (\cos^2 \delta \sin \beta) G_\delta + \frac{1}{\xi} (\cos \beta \cot \delta) G_\beta \right] = 0 \quad (A-9)$$

With $\xi \neq 0$, i.e., away from the conical apex, the conservative form is obtained as:

$$[E\xi]_\xi + [-\frac{1}{2} \sin 2\delta + (aF \cos \beta + bG \sin \beta) \cos^2 \delta]_\delta \\ + [(-aF \sin \beta + bG \cos \beta) \cot \delta]_\beta \quad (A-10) \\ + [(\cos 2\delta - 1)E + (aF \cos \beta + bG \sin \beta) (\cot \delta + \sin 2\delta)] = 0.$$

From Equation A-10, the matrix representation of the fluid flow equations in the computational polar system becomes:

$$\begin{bmatrix} E(pu) \\ E(P+pu^2) \\ E(puv) \\ E(puw) \end{bmatrix} + \begin{bmatrix} -\frac{1}{2}(pu) \sin 2\delta + (a(pv)\cos\beta + b(pw)\sin\beta)\cos^2\delta \\ -\frac{1}{2}(P+pu^2) \sin 2\delta + (a(puv)\cos\beta + b(puw)\sin\beta)\cos^2\delta \\ -\frac{1}{2}(puv) \sin 2\delta + (a(P+pv^2)\cos\beta + b(pvw)\sin\beta)\cos^2\delta \\ -\frac{1}{2}(puw) \sin 2\delta + (a(pvw)\cos\beta + b(P+pw^2)\sin\beta)\cos^2\delta \end{bmatrix} \quad (A-11)$$

$$+ \begin{bmatrix} (-a(pv)\sin\beta + b(pw)\cos\beta)\cot\delta \\ (-a(puv)\sin\beta + b(puw)\cos\beta)\cot\delta \\ (-a(P+pv^2)\sin\beta + b(pvw)\cos\beta)\cot\delta \\ (-a(pvw)\sin\beta + b(P+pw^2)\cos\beta)\cot\delta \end{bmatrix} \quad \beta$$

$$+ \begin{bmatrix} -2(pu)\sin^2\delta + (a(pv)\cos\beta + b(pw)\sin\beta)(\cot\delta + \sin 2\delta) \\ -2(P+pu^2)\sin^2\delta + (a(puv)\cos\beta + b(puw)\sin\beta)(\cot\delta + \sin 2\delta) \\ -2(puv)\sin^2\delta + (a(P+pv^2)\cos\beta + b(pvw)\sin\beta)(\cot\delta + \sin 2\delta) \\ -2(puw)\sin^2\delta + (a(pvw)\cos\beta + b(P+pw^2)\sin\beta)(\cot\delta + \sin 2\delta) \end{bmatrix} = 0$$

which has the general form of Equation A-8.

APPENDIX B: THE REFLECTION BOUNDARY CONDITION

The equation of the elliptic cone in Cartesian coordinates can be given by:

$$F(x, y, z) = \left(\frac{y}{b}\right)^2 + \left(\frac{z}{a}\right)^2 - \left(\frac{x}{c}\right)^2 = 0 \quad (B-1)$$

Due to the conical flow nature and the fact that the body may be replaced by a stream surface, the exact boundary condition is:

$$\vec{q} \cdot \vec{\nabla} F = 0, \text{ on the body,} \quad (B-2)$$

so that the velocity relationship that must be satisfied on the elliptic body surface is:

$$\frac{v}{u} = \frac{x}{y} \left(\frac{b}{c}\right)^2 - \frac{z}{y} \frac{w}{u} \left(\frac{b}{a}\right)^2 \quad (B-3)$$

An alternate way of expressing Equation B-2 must be found, so that the numerical method can be used. From the geometry of the problem, see Figure 1, it can be seen that:

$$\vec{q}_{\text{tan}} = \hat{i}_N \times (\vec{q} \times \hat{i}_N) \quad (B-4)$$

and

$$|\vec{q}_N| = \vec{q} \cdot \hat{i}_N \quad (B-5)$$

From calculus:

$$\hat{i}_N = \frac{\vec{\nabla F}}{|\vec{\nabla F}|} = \frac{[\frac{-x}{c^2}, \frac{y}{b^2}, \frac{z}{a^2}]}{[\frac{x^2}{c^4} + \frac{y^2}{b^4} + \frac{z^2}{a^4}]^{\frac{1}{2}}} \quad (B-6)$$

so that Equation B-4 becomes:

$$\begin{aligned} \vec{q}_{\tan} = \frac{1}{d^2} & \left\{ \left[\frac{y}{b^2} \left(\frac{uy}{b^2} + \frac{vx}{c^2} \right) + \frac{z}{a^2} \left(\frac{uz}{a^2} + \frac{wx}{c^2} \right) \right], \right. \\ & \left[\frac{x}{c^2} \left(\frac{uy}{b^2} + \frac{vx}{c^2} \right) + \frac{z}{a^2} \left(\frac{yz}{a^2} - \frac{wy}{b^2} \right) \right], \\ & \left. \left[\frac{x}{c^2} \left(\frac{uz}{a^2} + \frac{wx}{c^2} \right) - \frac{y}{b^2} \left(\frac{yz}{a^2} - \frac{wy}{b^2} \right) \right] \right\} \quad (B-7) \end{aligned}$$

and Equation B-5 becomes:

$$|\vec{q}_N| = \frac{1}{d} \left[-\frac{ux}{c^2} + \frac{vy}{b^2} + \frac{wz}{a^2} \right] \quad (B-8)$$

where

$$d = \left[\frac{x^2}{c^4} + \frac{y^2}{b^4} + \frac{z^2}{a^4} \right]^{\frac{1}{2}} \quad (B-9)$$

In the computational polar plane, Equations B-7, B-8, and B-9 become:

$$\vec{q}_{\tan} = \left(\frac{5}{d} \right) \left[\left(\frac{\tan^2 \delta \cos^2 \theta}{a^2 b^4} + \frac{\tan^2 \delta \sin^2 \theta}{a^4 h^2} \right) u + \frac{v \tan \delta \cos \theta}{b^2 c^2} + \frac{w \tan \delta \sin \theta}{a^2 b c^2} \right]$$

$$\left[\frac{u \tan \delta \cos \beta}{ab^2c^2} + \left(\frac{1}{c^4} + \frac{\tan^2 \delta \sin^2 \beta}{a^2b^2} \right) v - \frac{w \tan^2 \delta \cos \beta \sin \beta}{a^3b^3} \right],$$

$$\left[\frac{u \tan \delta \sin \beta}{a^2bc^2} - \frac{v \tan^2 \delta \cos \beta \sin \beta}{a^3b^3} + w \left(\frac{1}{c^4} + \frac{\tan^2 \delta \cos^2 \beta}{a^2b^2} \right) \right] \} \quad (B-10)$$

and

$$|\vec{q}_N| = \frac{1}{d} \left[\frac{-u}{c^2} + \frac{v \tan \delta \cos \beta}{ab^2} + \frac{w \tan \delta \sin \beta}{a^2b} \right] \quad (B-11)$$

where

$$d = \left[\frac{1}{c^4} + \frac{\tan^2 \delta}{a^2b^2} \left(\frac{\cos^2 \beta}{b^2} + \frac{\sin^2 \beta}{a^2} \right) \right] \quad (B-12)$$

The reflection boundary condition chosen assumes:

$$|\vec{q}_N|^+ = -|\vec{q}_N|^- \quad (B-13)$$

and

$$|\vec{q}_{\tan}|^+ = |\vec{q}_{\tan}|^- \quad (B-14)$$

where the (+) sign indicates the values at the first mesh layer above the body (superlayer), and the (-) sign indicates values at the first mesh layer below the body (sub-layer). This component reflection can be visualized as:

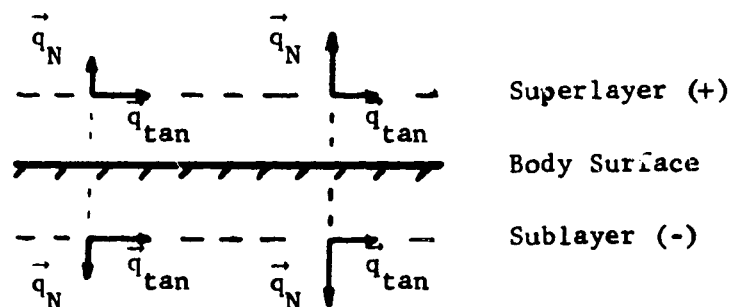


Figure B-1: Component Reflection.

Equations B-10 and B-11 actually yield an overdetermined system. Since there are only three unknowns (u^- , v^- and w^-), only three relations are needed. Let:

$$\vec{q}_{\text{tan}} = \frac{1}{d^2} (|\vec{q}_{\text{tan}}|_1, |\vec{q}_{\text{tan}}|_2, |\vec{q}_{\text{tan}}|_3) \quad , \quad (\text{B-15})$$

which has form identical to Equation B-10. The system of three equations necessary to solve for the three unknowns is:

$$|\vec{q}_N|^+ = -|\vec{q}_N|^- \quad (\text{B-16})$$

$$|\vec{q}_{\text{tan}}|_1^+ = |\vec{q}_{\text{tan}}|_1^- \quad (\text{B-17})$$

$$|\vec{q}_{\text{tan}}|_2^+ = |\vec{q}_{\text{tan}}|_2^- \quad (\text{B-18})$$

Thus from Equations B-10 and B-11 the following is acquired for the boundary condition relation:

$$\pm |\vec{q}_N| = \frac{\epsilon}{d^{\pm}} \left[\frac{-u^{\pm}}{c^2} + \frac{\tan \delta^{\pm}}{ab} \left(\frac{v^{\pm} \cos \beta}{b} + \frac{w^{\pm} \sin \beta}{a} \right) \right] \quad (\text{B-19})$$

$$|\vec{q}_{\tan}|_2^{\pm} = \left(\frac{\epsilon}{d^{\pm}} \right)^2 \left[\frac{u^{\pm} \tan \delta^{\pm} \cos \beta}{ab^2 c^2} + \left(\frac{1}{c^4} + \frac{\tan^2 \delta^{\pm} \sin \beta}{a^4 b^2} \right) v^{\pm} - \frac{w^{\pm} \tan^2 \delta^{\pm} \cos \beta \sin \beta}{a^3 b^3} \right] \quad (\text{B-20})$$

$$|\vec{q}_{\tan}|_3^{\pm} = \left(\frac{\epsilon}{d^{\pm}} \right)^2 \left[\frac{u^{\pm} \tan^2 \delta^{\pm} \sin \beta}{a^2 b c^2} - \frac{v^{\pm} \tan^2 \delta^{\pm} \cos \beta \sin \beta}{a^3 b^3} + \left(\frac{1}{c^4} + \frac{\tan^2 \delta^{\pm} \cos^2 \beta}{a^2 b^4} \right) w^{\pm} \right] \quad (\text{B-21})$$

where the (+) superscript indicates that the variables are evaluated at the superlayer and the (-) superscript indicated evaluation at the sublayer.

Equations B-19, B-20 and B-21 constitute a system of three equations and three unknowns which, when written in matrix form, become:

$$\begin{bmatrix} -\frac{1}{c^2} & \frac{\tan \delta^- \cos \beta}{ab^2} & \frac{\tan \delta^- \sin \beta}{a^2 b} \\ \frac{\tan \delta^- \cos \beta}{ab^2 c^2} & \frac{1}{c^4} + \frac{\tan^2 \delta^- \sin \beta}{a^4 b^2} & -\frac{\tan^2 \delta^- \cos \beta \sin \beta}{a^3 b^3} \\ \frac{\tan \delta^- \sin \beta}{a^2 b c^2} & -\frac{\tan^2 \delta^- \cos \beta \sin \beta}{a^3 b^3} & \frac{1}{c^4} + \frac{\tan^2 \delta^- \cos^2 \beta}{a^2 b^4} \end{bmatrix} \begin{bmatrix} u^- \\ v^- \\ w^- \end{bmatrix}$$

$$= \begin{bmatrix} -|\vec{q}_N| & \frac{d^-}{s} \\ |\vec{q}_{\tan}|_2 & (\frac{d^-}{s})^2 \\ |\vec{q}_{\tan}|_3 & (\frac{d^-}{s})^2 \end{bmatrix} \quad (B-22)$$

Cramer's rule can now be applied to Equation B-22 to determine the desired values of u^- , v^- , and w^- .

Pressure and density are assumed to be even functions across the body boundary so that their normal derivative can be set equal to zero. This yields the pressure and density boundary conditions:

$$p^+ = p^- \quad (B-23)$$

and

$$\rho^+ = \rho^- \quad (B-24)$$

APPENDIX C: THE ENTROPY BOUNDARY CONDITION

From the explicit predictor, P_1 , ρ_1 , u_1 , v_1 , and w_1 are known, while P_2 , ρ_2 , u_2 , v_2 and w_2 on the body are desired. The assumption is that since the predictor has only first order accuracy, $\vec{q}_1 = (u_1, v_1, w_1)$ on the body will not be parallel to the body surface as dictated by the exact boundary condition, Equation B-2. Instead, \vec{q}_1 will be canted at an angle, $\pm\Delta\theta$, with respect to \vec{q}_{tan} , thus giving rise to a normal velocity component at the body surface. This result does not satisfy the boundary conditions given by Equations B-2 and B-3. To rectify this, the entropy boundary condition used by Abbett (1) provides a local compression or expansion, depending on $\pm\Delta\theta$ to "bring" \vec{q}_1 back to tangency.

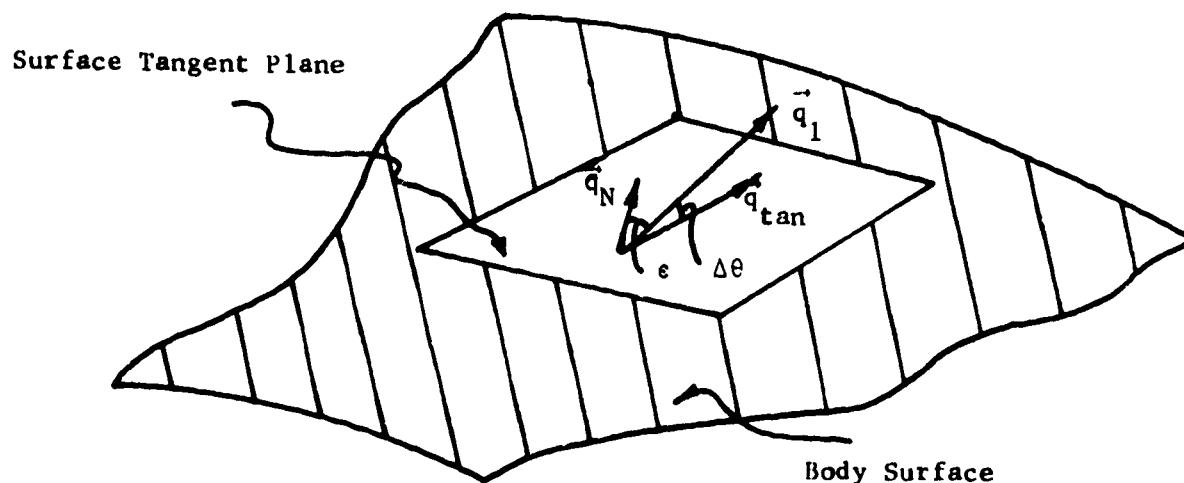


Figure C-1 Velocity vector geometry.

From Figure C-1, it is seen that:

$$\frac{\vec{q}_1}{|\vec{q}_1|} \cdot \hat{i}_N = \cos \epsilon = \sin(\Delta\theta) \quad (C-1)$$

so that,

$$\Delta\theta = \sin^{-1} \left[\frac{\vec{q}_1}{|\vec{q}_1|} \cdot \hat{i}_N \right] \quad (C-2)$$

where $+\Delta\theta$ denotes an expansion and $-\Delta\theta$ denotes a compression. Carrying out the operation indicated in Equation C-2 yields:

$$\Delta\theta = \sin^{-1} \left[\frac{-\frac{u_1}{c} \frac{x}{d} + \frac{v_1}{b} \frac{y}{d} + \frac{w_1}{a} \frac{z}{d}}{|\vec{q}_1|} \right] \quad (C-3)$$

where d is defined by Equation B-9 and \hat{i}_N is as in Equation B-6.

From NACA R-1135 (15), the static pressure after turning the flow parallel to the body is determined by:

$$P_2 = P_1 \left[1 - \frac{\gamma M_1^2 (\Delta\theta)^2}{(M_1^2 - 1)^2} + \frac{M_1^2 (\gamma + 1) M_1^4 - 4 (M_1^2 - 1) (\Delta\theta)^2}{4 (M_1^2 - 1)^2} + O(\Delta\theta)^3 \right] \quad (C-4)$$

where M_1 is found from:

$$M_1 = \frac{|\vec{q}_1|}{a_1} = \frac{|\vec{q}_1|}{\left(\frac{\gamma P_1}{\rho_1}\right)^{1/2}} = \left[\frac{(u_1^2 + v_1^2 + w_1^2)}{\left(\frac{P_1 \gamma}{\rho_1}\right)} \right]^{1/2}. \quad (C-5)$$

Note: P_1 , ρ_1 , M_1 , $|\vec{q}_1|$, and a_1 are all nondimensional variables as defined in Appendix E, unless otherwise specified.

From the equation of state, $\rho_2 = \rho_2(S, P_2)$, so that:

$$\frac{P_1}{\rho_1^\gamma} = \frac{P_2}{\rho_2^\gamma} = \text{constant}, \quad (C-6)$$

which yields the relation for the density:

$$\rho_2 = \rho_1 \left[\frac{P_2}{P_1} \right]^{\frac{1}{\gamma}}, \quad (C-7)$$

where P_1 and ρ_1 are obtained from the plane containing the crossflow stagnation point. For zero angle of attack, the crossflow stagnation point coincides with the $\beta = 90^\circ$ plane (see Figure 1).

From the energy equation, total enthalpy is found as:

$$h_T = \frac{\gamma}{\gamma-1} \left[\frac{P_{\infty T}}{P_T} \right] = \frac{\gamma}{\gamma-1} \left[\frac{P}{P} \right] + \frac{|\vec{q}|^2}{2} \quad (C-8)$$

which yields the velocity modulus, $|\vec{q}_2|$:

$$|\vec{q}_2| = \left[\frac{2}{\gamma-1} \left(1 - \frac{P_2 \gamma}{P_1} \right) \right]^{\frac{1}{2}} . \quad (C-9)$$

Note: In Equation C-8, P , P , and $|\vec{q}|$ are in dimensional form.

Thus, the magnitude of the velocity vector tangent to the surface is found. In order to determine \vec{q}_2 , a unit vector in the direction of \vec{q}_2 is defined as:

$$\hat{i}_{q_2} \triangleq \frac{u_2, v_2, w_2}{|\vec{q}_2|} = \frac{u_2^i, v_2^i, w_2^i}{|\vec{q}_2^i|} . \quad (C-10)$$

From Figure C-1,

$$\vec{q}_2 = \vec{q}_{\tan} \approx \vec{q}_2^o = \vec{q}_1 - (\vec{q}_1 \cdot \hat{i}_N) \hat{i}_N . \quad (C-11)$$

Therefore, \vec{q}_2^o is in the direction of \vec{q}_2 , but it is not necessarily true that $|\vec{q}_2^o| = |\vec{q}_2|$, due to truncation error. The unit vector, \hat{i}_{q_2} , can now be formed as:

$$\hat{i}_{q_2} = \frac{\vec{q}_2^o}{|\vec{q}_2^o|} \quad (C-12)$$

Carrying out the operations indicated in Equation C-11 yields:

$$\begin{aligned} \vec{q}_2^0 = \left\{ \left[u_1 - \frac{1}{d^2} \left(\frac{u_1 x^2}{c^2} - \frac{v_1 xy}{b^2 c^2} - \frac{w_1 xz}{a^2 c^2} \right) \right], \right. \\ \left[v_1 - \frac{1}{d^2} \left(-\frac{u_1 xy}{b^2 c^2} + \frac{v_1 y^2}{b^4} + \frac{w_1 yz}{a^2 b^2} \right) \right], \\ \left. \left[w_1 - \frac{1}{d^2} \left(-\frac{u_1 xz}{a^2 c^2} + \frac{v_1 yz}{a^2 b^2} + \frac{w_1 z^2}{a^4} \right) \right] \right\}, \end{aligned} \quad (C-13)$$

where d is as in Equation B-9. Finally,

$$\vec{q}_2 = |\vec{q}_2| \frac{\vec{q}_2^0}{|\vec{q}_2^0|} = |\vec{q}_2| \hat{i}_{q_2} \quad (C-14)$$

can be calculated.

Since numerical computation is performed in the computational polar system, the appropriate equations above must be transformed using Equations A-1, A-4, A-5 and A-6. This yields:

$$\Delta\theta = \sin^{-1} \left\{ \frac{\left[-\frac{u_1}{c^2} + \frac{\tan\delta}{ab} \left(\frac{v_1 \cos\delta}{b} + \frac{w_1 \sin\delta}{a} \right) \right]}{\left[(u_1^2 + v_1^2 + w_1^2) \left(\frac{1}{c^2} + \frac{\tan^2\delta}{a^2 b^2} \left(\frac{\cos^2\delta}{b^2} + \frac{\sin^2\delta}{a^2} \right) \right) \right]^{\frac{1}{2}}} \right\} \quad (C-15)$$

and since $\vec{q}_2^0 = (u_2^0, v_2^0, w_2^0)$:

$$u_2^0 = u_1 - \left(\frac{\xi}{d}\right)^2 \left[\frac{u_1}{c^4} - \frac{v_1 \tan \delta \cos \beta}{ab^2 c^2} - \frac{w_1 \tan \delta \sin \beta}{a^2 bc^2} \right] \quad (C-16)$$

$$v_2^0 = v_1 - \left(\frac{\xi}{d}\right)^2 \left[\frac{u_1 \tan \delta \cos \beta}{ab^2 c^2} - \frac{v_1 \tan^2 \delta \cos^2 \beta}{a^2 b^4} - \frac{w_1 \tan^2 \delta \cos \beta \sin \beta}{a^3 b^3} \right] \quad (C-17)$$

$$w_2^0 = w_1 - \left(\frac{\xi}{d}\right)^2 \left[\frac{u_1 \tan \delta \sin \beta}{a^2 bc^2} - \frac{v_1 \tan^2 \delta \cos \beta \sin \beta}{a^3 b^3} - \frac{w_1 \tan^2 \delta \sin \beta}{a^4 b^2} \right] \quad (C-18)$$

where d is from Equation B-12. Finally,

$$u_2 = \frac{u_2^0}{|\vec{q}_2^0|} |\vec{q}_2| = \frac{u_2^0}{|\vec{q}_2^0|} \left[\frac{2}{\gamma-1} \left(1 - \frac{P_2 \gamma}{\rho_2} \right) \right]^{\frac{1}{2}} \quad (C-19)$$

and likewise,

$$v_2 = \frac{v_2^0}{|\vec{q}_2^0|} |\vec{q}_2| \quad \text{and} \quad w_2 = \frac{w_2^0}{|\vec{q}_2^0|} |\vec{q}_2| \quad (C-20, 21)$$

The crossflow stagnation points are located at the points where $\vec{q}_C = 0$. The derivation for the radial and crossflow velocity components are now presented.

From Figure 1, it can be seen that:

$$\begin{aligned}\vec{R} &= (x, y, z) \\ \hat{i}_C &= \hat{i}_R \times \hat{i}_N\end{aligned}\quad (C-22)$$

where \hat{i}_N is from Equation B-6 and

$$\hat{i}_R = \frac{\vec{R}}{|\vec{R}|} = \frac{(x, y, z)}{(x^2 + y^2 + z^2)^{\frac{1}{2}}}, \quad (C-23)$$

so that,

$$\hat{i}_C = \hat{i}_R \times \hat{i}_N = \frac{1}{Dd} \left[\left(\frac{YZ}{a^2} - \frac{YZ}{b^2} \right), \left(-\frac{XZ}{a^2} - \frac{XZ}{c^2} \right), \left(\frac{XY}{b^2} + \frac{XY}{c^2} \right) \right] \quad (C-24)$$

where d is from Equation B-9 and

$$D = (x^2 + y^2 + z^2)^{\frac{1}{2}}. \quad (C-25)$$

From Figure 1, it can be seen that:

$$|\vec{q}_C| = \vec{q} \cdot \hat{i}_C \quad (C-26)$$

and

$$|\vec{q}_R| = \vec{q} \cdot \hat{i}_R \quad (C-27)$$

However, since numerical computation is again performed on the computational polar system, the transformation equations, Equations A-1, A-4, A-5 and A-6, must be applied to Equations C-26 and C-27. Carrying out the indicated operations, Equations

tion C-26 becomes:

$$|\vec{q}_C| = \frac{\tan \delta \left[\frac{u(b^2 - a^2) \tan \delta \cos \beta \sin \beta}{a^3 b^3} - \frac{v(a^2 + c^2) \sin \beta}{a^2 b c^2} + \frac{w(b^2 + c^2) \cos \beta}{a b^2 c^2} \right]}{\left[1 + \tan^2 \delta \left(\frac{\cos^2 \beta}{a^2} + \frac{\sin^2 \beta}{b^2} \right) \right]^{\frac{1}{2}} \left[\frac{1}{c^4} + \frac{\tan^2 \delta}{a^2 b^2} \left(\frac{\cos^2 \beta}{b^2} + \frac{\sin^2 \beta}{a^2} \right) \right]^{\frac{1}{2}}} \quad (C-28)$$

and Equation C-27 becomes:

$$|\vec{q}_R| = \frac{u + \tan \delta \left(\frac{v \cos \beta}{a} + \frac{w \sin \beta}{b} \right)}{\left[1 + \tan^2 \delta \left(\frac{\cos^2 \beta}{a^2} + \frac{\sin^2 \beta}{b^2} \right) \right]^{\frac{1}{2}}} \quad (C-29)$$

APPENDIX D: EIGENVALUES

The matrix form of the governing partial differential equations of fluid flow in the Cartesian system is written as:

$$\tilde{A}\tilde{u}_{\xi} + \tilde{B}\tilde{u}_{\delta} + \tilde{C}\tilde{u}_{\beta} = 0 \quad . \quad (D-1)$$

However, to acquire a form amenable to the MacCormack second order predictor-corrector technique in the computational polar system, Equation D-1 must be rewritten into the form:

$$\tilde{u}_{\xi} + A^{-1}\tilde{B}\tilde{u}_{\delta} + A^{-1}\tilde{C}\tilde{u}_{\beta} = 0 \quad , \quad (D-2)$$

where A , \tilde{A} , B , \tilde{B} , C and \tilde{C} are $n \times n$ matrices, n being the order of the system, and $\tilde{u}^T = (u, v, w, P, \rho)$.

To derive Equation D-2, transformations must be made from the Cartesian system to the computational polar system using the chain rule and the transformation Equations A-1, A-4, A-5 and A-6. In this manner, Equation D-2 becomes:

$$\tilde{u}_{\xi} + [\delta_x + aA^{-1}\tilde{B}\delta_y + bA^{-1}\tilde{C}\delta_z]\tilde{u}_{\delta} + [aA^{-1}\tilde{B}\beta_y + bA^{-1}\tilde{C}\beta_z]\tilde{u}_{\beta} = 0 \quad , \quad (D-3)$$

where

$$\begin{aligned}
 A &= \tilde{A} \\
 B &= \tilde{A} \delta_{x'} + a \tilde{B} \delta_{y'} + b \tilde{C} \delta_{z'} \quad (D-4)
 \end{aligned}$$

and

$$C = a \tilde{B} \beta_{y'} + b \tilde{C} \beta_{z'} .$$

Now the matrices $A^{-1} \tilde{B}$ and $A^{-1} \tilde{C}$ must be found. The partial differential equations of fluid flow:

$$\text{X-Momentum: } (P + \rho u^2)_x + (\rho uv)_y + (\rho uw)_z = 0 \quad (D-5)$$

$$\text{Y-Momentum: } (\rho uv)_x + (P + \rho v^2)_y + (\rho vw)_z = 0 \quad (D-6)$$

$$\text{Z-Momentum: } (\rho uw)_x + (\rho vw)_y + (P + \rho w^2)_z = 0 \quad (D-7)$$

$$\text{Energy: } \vec{q} \cdot (\vec{\nabla} P - c^2 \vec{\nabla} \rho) = 0 \quad (D-8)$$

$$\text{Continuity: } \nabla \cdot (\rho \vec{q}) = 0 \quad , \quad (D-9)$$

where from Kutler (14), $c^2 = \left(\frac{\partial P}{\partial \rho} \right)_S$, yield the matrices \tilde{A} , \tilde{B} and \tilde{C} . The desired quantities are then obtained as:

$$A = \begin{bmatrix} \frac{c^2 + u^2}{(c^2 - u^2)} \rho & \frac{-u}{(c^2 - u^2)} \rho & 0 & 0 & \frac{1}{\rho(c^2 - u^2)} \\ -\frac{v}{u} & 0 & \frac{1}{u} & 0 & 0 \\ -\frac{u}{u} & 0 & 0 & \frac{1}{u} & 0 \\ \frac{-2uc^2}{c^2 - u^2} & \frac{c^2}{c^2 - u^2} & 0 & 0 & \frac{-u}{c^2 - u^2} \\ \frac{-2u}{c^2 - u^2} & \frac{1}{c^2 - u^2} & 0 & 0 & \frac{-1}{u(c^2 - u^2)} \end{bmatrix} \quad (D-10)$$

$$A^{-1} \tilde{B} = \begin{bmatrix} \frac{-uv}{c^2 - u^2} & \frac{c^2}{c^2 - u^2} & 0 & \frac{v}{\rho(c^2 - u^2)} & 0 \\ 0 & \frac{v}{u} & 0 & \frac{1}{\rho u} & 0 \\ 0 & 0 & \frac{v}{u} & 0 & 0 \\ \frac{\rho v c^2}{c^2 - u^2} & \frac{-\rho u c^2}{c^2 - u^2} & 0 & \frac{-uv}{c^2 - u^2} & 0 \\ \frac{\rho v}{c^2 - u^2} & \frac{-\rho u}{c^2 - u^2} & 0 & \frac{-v}{u(c^2 - u^2)} & \frac{v}{u} \end{bmatrix} \quad (D-11)$$

and

$$A^{-1} \tilde{C} = \begin{bmatrix} \frac{-uv}{c^2 - u^2} & 0 & \frac{c^2}{c^2 - u^2} & \frac{w}{\rho(c^2 - u^2)} & 0 \\ 0 & \frac{w}{u} & 0 & 0 & 0 \\ 0 & 0 & \frac{w}{u} & \frac{1}{u} & 0 \\ \frac{\rho w c^2}{c^2 - u^2} & 0 & \frac{-\rho u c^2}{c^2 - u^2} & \frac{-uw}{c^2 - u^2} & 0 \\ \frac{\rho w}{c^2 - u^2} & 0 & \frac{-\rho u}{c^2 - u^2} & \frac{-w}{u(c^2 - u^2)} & \frac{w}{u} \end{bmatrix} \quad (D-12)$$

utilizing Equations A-1, A-4, A-5 and A-6, Equations D-4 can be rewritten as:

$$\begin{aligned} A &= \tilde{A} \\ B &= -\frac{I}{\xi} \cos \delta \sin \delta + \frac{a}{\xi} A^{-1} \tilde{B} \cos^2 \delta \cos \beta + \frac{b}{\xi} A^{-1} \tilde{C} \cos^2 \delta \sin \beta \\ C &= -\frac{a}{\xi} A^{-1} \tilde{B} \cot \delta \sin \beta + \frac{b}{\xi} A^{-1} \tilde{C} \cot \delta \cos \beta \end{aligned} \quad (D-13)$$

The eigenvalues, and eventually the linear stability bounds, are found by solving the characteristic equations:

$$\det (B - \sigma I) = 0 \quad (D-14)$$

and

$$\det (C - \lambda I) = 0 \quad (D-15)$$

and obtaining the characteristic roots. The resulting eigenvalues are:

$$\sigma_{1,2,3} = \frac{-\cos\delta \sin\delta}{\xi} + \frac{\cos^2\delta}{u\xi} (av\cos\beta + bv\sin\beta) \quad (D-16)$$

$$\begin{aligned} \sigma_{4,5} = & \left[-[(av\cos\beta + bv\sin\beta) \frac{u\cos\delta}{(c^2-u^2)} + \sin\delta] \right. \\ & \pm \left\{ [(av\cos\beta + bv\sin\beta) \frac{u\cos\delta}{(c^2-u^2)} + \sin\delta]^2 \right. \\ & \left. - \sin^2\delta - 2(av\cos\beta + bv\sin\beta) \frac{u\cos\delta \sin\delta}{(c^2-u^2)} \right. \\ & \left. + (av\cos\beta + bv\sin\beta)^2 \frac{\cos^2\delta}{(c^2-u^2)} \right. \\ & \left. - (a^2\cos^2\beta + b^2\sin^2\beta) \frac{c^2\cos^2\delta}{(c^2-u^2)} \right\}^{\frac{1}{2}} \left. \right] \frac{\cos\delta}{\xi} \quad (D-17) \end{aligned}$$

and

$$\lambda_{1,2,3} = (bv\cos\beta - av\sin\beta) \frac{\cot\delta}{u\xi} \quad (D-18)$$

$$\begin{aligned} \lambda_{4,5} = & \left[(av\sin\beta - bv\cos\beta) \frac{u}{(c^2-u^2)} \right. \\ & \pm \left\{ (av\sin\beta - bv\cos\beta)^2 \frac{u}{(c^2-u^2)} \right. \\ & \left. + (av\sin\beta - bv\cos\beta)^2 \frac{1}{(c^2-u^2)} \right. \\ & \left. - (a^2\sin^2\beta + b^2\cos^2\beta) \frac{c^2}{(c^2-u^2)} \right\}^{\frac{1}{2}} \left. \right] \frac{\cot\delta}{\xi} \quad (D-19) \end{aligned}$$

APPENDIX E: NONDIMENSIONALIZATION AND INITIAL CONDITIONS

Nondimensionalization

The dimensional flow variables \bar{P} , $\bar{\rho}$, \bar{u} , \bar{v} and \bar{w} are nondimensionalized to P , ρ , u , v and w as follows:

$$P = \frac{\bar{P}}{\gamma \bar{P}_{\infty T}} \quad (E-1)$$

$$\rho = \frac{|\bar{\rho}|}{\bar{\rho}_{\infty T}} \quad (E-2)$$

$$u, v, w = \frac{\bar{u}, \bar{v}, \bar{w}}{\left[\frac{\gamma \bar{P}_{\infty T}}{\bar{\rho}_{\infty T}} \right]^{\frac{1}{2}}} \quad (E-3, 4, 5)$$

Initial Conditions

From NACA R-1135 (15);

$$\frac{P}{P_{\infty T}} = \left[1 + \frac{(\gamma-1)}{2} M_{\infty}^2 \right]^{\frac{-\gamma}{\gamma-1}} \Rightarrow P = \frac{1}{\gamma} \left[1 + \frac{(\gamma-1)}{2} M_{\infty}^2 \right]^{\frac{-\gamma}{\gamma-1}} \quad (E-6)$$

$$\frac{\rho}{\rho_{\infty T}} = \left[1 + \frac{(\gamma-1)}{2} M_{\infty}^2 \right]^{\frac{-1}{\gamma-1}} \Rightarrow \rho = \left[1 + \frac{(\gamma-1)}{2} M_{\infty}^2 \right]^{\frac{-1}{\gamma-1}} \quad (E-7)$$

$$\frac{q}{q_{\infty}} = \left[1 + \frac{(\gamma-1)}{2} M_{\infty}^2 \right]^{\frac{1}{2}} \Rightarrow q = M_{\infty} \left[1 + \frac{(\gamma-1)}{2} M_{\infty}^2 \right]^{\frac{1}{2}} \quad (E-8)$$

since

$$\bar{P} = \left[\frac{\gamma \bar{P}}{\bar{\rho}} \right]^{\frac{1}{2}} \quad (E-9)$$

APPENDIX F: INVERSION

From Appendix A, Equation A-11, define:

$$E_1 = \xi \rho u \quad (F-1)$$

$$E_2 = \xi(P + \rho u^2) \quad (F-2)$$

$$E_3 = \xi \rho u v \quad (F-3)$$

$$E_4 = \xi \rho u w \quad (F-4)$$

then the flow variables can be found as:

$$v = \frac{E_3}{E_1} \quad (F-5)$$

$$w = \frac{E_4}{E_1} \quad (F-6)$$

$$u = \frac{E_2 \pm \left\{ E_2^2 - 4 E_1^2 \left[1 - \frac{(\gamma-1)}{2\gamma} \right] \left[\frac{1}{\gamma} - \frac{(\gamma-1)}{2\gamma} (v^2 + w^2) \right] \right\}^{\frac{1}{2}}}{\frac{E_1 (\gamma+1)}{\gamma}} \quad (F-7)$$

$$\rho = \frac{E_1}{u \xi} \quad (F-8)$$

$$P = \frac{E_2}{\xi} - \rho u^2 \quad (F-9)$$

The (+) sign in Equation F-7 is used because the flow is supersonic.

APPENDIX *B

This is a preprint of a paper intended for publication in a journal or proceedings. Since changes may be made before publication, this preprint is made available with the understanding that it will not be cited or reproduced without the permission of the author.

ERI - 72118

PREPRINT

Project 911-S

Engineering Research Institute

IOWA STATE UNIVERSITY

AMES

NUMERICAL SOLUTIONS OF THE ADVECTION EQUATION USING CONSERVATIVE FORM

Dale Anderson and Behrooz Fattahi

April 1972

This paper was prepared for submission to
The Journal of Applied Meteorology

NUMERICAL SOLUTIONS OF THE ADVECTION EQUATION
USING CONSERVATIVE FORM

Dale Anderson and Behrooz Fattahi
Department of Aerospace Engineering and
Engineering Research Institute
Iowa State University, Ames, Iowa 50010

Abstract

Second- and third-order finite difference methods recently applied to problems in high speed fluid flow are applied to the model advection equation cast in conservative form. The differencing methods considered use forward time differencing with preferential space differences employed in the predictor-corrector sequences. The free parameter required for stability in the third-order method is adjusted to cause the solution to be either minimum dispersive or minimum dissipative in nature. Results indicate that the third-order method using minimum dissipation is the most accurate method tested. Computer time requirements are approximately twice those needed for second-order techniques.

1. Introduction

Numerical integration of the equations describing atmospheric motion has become commonplace since the advent of the high-speed digital computer. Techniques used in performing this integration have varied widely in order of accuracy, programming ease and computation time required. This paper deals with application of recently developed second- and third-order techniques to the advection process using the differential equations describing advection in conservative form.

The accuracy with which a finite difference method models advection within the atmosphere is difficult to assess since the governing equations are extremely nonlinear. Molenkamp (1968) has suggested that representative numerical methods be applied to a simple problem whose exact solution is known in order to compare the results obtained through the use of each technique. The results of his investigation show that higher order numerical methods more accurately model the advection process. Molenkamp concludes that of the methods tested, the Roberts and Weiss (1966) technique most nearly approximates the exact solution. This method is fourth-order in space and second-order in time. The disadvantage lies in the fact that it requires at least one more order of magnitude in computing time and considerably more storage space than, for example, a Lax-Wendroff second-order scheme.

Crowley (1968) has performed a similar analysis including a comparison of the accuracy of solutions obtained using advective form and conservative form of the describing equations. These results were obtained for longer integration times but generally agree with those of Molenkamp.

In addition, Crowley concludes that the conservative form of the governing equation is preferred over the advective form.

The test problem which Crowley and Molenkamp have used assumes that advection of a quantity A is governed by the differential equation

$$\frac{\partial A}{\partial t} = -u \frac{\partial A}{\partial x} - v \frac{\partial A}{\partial y} \quad (1)$$

where u and v are the velocity components in the x and y directions and t is the time. This equation can be put in conservative form if the divergence of the velocity vanishes as

$$\frac{\partial u}{\partial x} + \frac{\partial v}{\partial y} = 0. \quad (2)$$

The nonhomogeneous terms vanish and the conservative form of (1) becomes

$$\frac{\partial A}{\partial t} + \frac{\partial (uA)}{\partial x} + \frac{\partial (vA)}{\partial y} = 0. \quad (3)$$

The conservative form (3) and the advective form (1) describe the same physical phenomena (assuming $\text{Div } \vec{V} = 0$) and should provide the same solution for a given set of initial data. Since numerical solutions are obtained on a finite grid, the solutions to (1) and (3) are different except in the limiting case as Δt , Δx and Δy approach zero.

A particularly simple model of the advection process can be studied when the velocity field is prescribed and due to a rigid body rotation of angular velocity Ω about some axis. In this case, the advective form may be written in polar coordinates as

$$\frac{\partial A}{\partial t} + \Omega \frac{\partial A}{\partial \theta} = 0 \quad (4)$$

where θ is the angular coordinate. This is just the simple one-dimensional wave equation which has the solution

$$A(r, \theta, t) = A_0(r, \theta - \Omega t) \quad (5)$$

where r is the polar radius measured from the axis of rotation and A_0 is the initial distribution of A . The initial distribution is rotated through angle Ωt . This is the correct solution to either the advective form or the conservative form of the governing equation.

Application of numerical differencing methods to this simple problem provides a rough comparison of the usefulness of the methods in modeling the advection process. Unfortunately, the velocity field usually depends upon t and is coupled complexly to the advected quantity A in the real problem. However, by solving the numerical problem in a rectangular coordinate system, some of the nonlinear character of the original problem is retained.

In the following sections, several numerical techniques are reviewed which have been applied to high speed gas dynamic and aerodynamic problems with great success. Phase error and amplitude plots are constructed and the methods are applied to the conservative form of the advection equation. The results obtained are compared with those of Molenkamp and Crowley.

2. Differencing Methods

The numerical techniques used in this study have been developed for hyperbolic systems of the form:

$$\frac{\partial E}{\partial t} + \frac{\partial F}{\partial x} = 0 \quad (6)$$

where E and F may be N component vectors and x may be of arbitrary dimension. The techniques are based upon the Runge-Kutta method and are explicit in advancing the solution forward in time.

MacCormack's Method MacCormack (1969) developed a noncentered second-order method which has been used extensively in solving gas dynamic problems involving strong shock waves. This technique consists of a two-step predictor-corrector sequence of the form

$$\tilde{E}_j^{n+1} = E_j^n - \frac{\Delta T}{\Delta x} (1 - \epsilon \Delta) \Delta F_j^n \quad (7)$$

$$E_j^{n+1} = \frac{1}{2} [E_j^n + \tilde{E}_j^{n+1}] - \frac{1}{2} \frac{\Delta T}{\Delta x} (1 + \epsilon \Delta) \Delta \tilde{F}_j^{n+1} \quad (8)$$

where the tilde represents values at the intermediate step and

$$\begin{aligned} \Delta F_j &= F_{j+1} - F_j \\ \nabla F_j &= F_j - F_{j-1} \end{aligned} \quad (9)$$

The value of ϵ can be either 0 or 1. If $\epsilon = 0$, the predictor uses a forward difference and the corrector uses a backward difference on F_j . If $\epsilon = 1$, the differencing in the predictor and corrector are reversed.

This method was derived using staggered differencing with the constraint that both left and right moving waves be properly computed. In addition, the method satisfies the perfect shift condition. If the simple one-dimensional wave equation is considered

$$\frac{\partial u}{\partial t} + c \frac{\partial u}{\partial x} = 0 \quad (10)$$

a solution may be written

$$u(x, t) = u(x - c\Delta t, t) . \quad (11)$$

If $\nu = \frac{c\Delta t}{\Delta x}$, then it follows that

$$u(x, t) = u(x - \nu\Delta x, t) . \quad (11A)$$

For a finite difference mesh the perfect shift condition

$$u_j^{n+1} = u_{j \pm m}^n \quad \nu = \pm m, m = 1, 2, \dots \quad (12)$$

is satisfied where ν is the Courant number.

MacCormack's method can be viewed as a version of the Lax-Wandroff method. The use of noncentered differences is advantageous since only values on the mesh points need be computed. This eliminates difficulties encountered in storage shifting and results in a considerable reduction in computer time. Kutler, Lomax and Warming have recently extended this method so the predictor can be evaluated at any fractional time step. Only values at $(n + 1)\Delta t$ were used in this study.

MacCormack's method is readily extended to two-space dimensions and when applied to (3) becomes:

$$\begin{aligned} \tilde{A}_{i,j}^{n+1} = & A_{i,j}^n - \frac{\Delta T}{\Delta x} \left[(1 - \epsilon_x)(uA)_{i+1,j}^n - (1 - 2\epsilon_x)(uA)_{i,j}^n \right. \\ & \left. - \epsilon_x(uA)_{i-1,j}^n \right] - \frac{\Delta T}{\Delta y} \left[(1 - \epsilon_y)(vA)_{i,j+1}^n \right. \\ & \left. - (1 - 2\epsilon_y)(vA)_{i,j}^n - \epsilon_y(vA)_{i,j-1}^n \right] \end{aligned} \quad (13)$$

$$\begin{aligned}
A_{i,j}^{n+1} = & \frac{1}{2} \left[A_{i,j}^n + \tilde{A}_{i,j}^{n+1} \right] - \frac{1}{2} \left\{ \frac{\Delta T}{\Delta x} \left[\epsilon_x (\tilde{uA})_{i+1,j}^{n+1} + (1 - 2\epsilon_x) (\tilde{uA})_{i,j}^{n+1} \right. \right. \\
& + (\epsilon_x - 1) (\tilde{uA})_{i-1,j}^{n+1} \left. \right] + \frac{\Delta T}{\Delta z} \left[\epsilon_y (\tilde{vA})_{i,j+1}^{n+1} \right. \\
& \left. \left. + (1 - 2\epsilon_y) (\tilde{vA})_{i,j-1}^{n+1} + (\epsilon_y - 1) (\tilde{vA})_{i,j-1}^{n+1} \right] \right\} \quad (13A)
\end{aligned}$$

Since the ϵ parameter can change in both the x and y direction, a question arises in selecting the best values of the ϵ 's to use. MacCormack (1971) suggests that the values of ϵ_x and ϵ_y be cyclically permuted to obtain results which are spatially unbiased. The allowable values of the ϵ 's are:

$$\begin{array}{ll}
\epsilon_x = 1 & \epsilon_y = 1 \\
\epsilon_x = 1 & \epsilon_y = 1 \\
\epsilon_x = 0 & \epsilon_y = 1 \\
\epsilon_x = 0 & \epsilon_y = 0
\end{array} \quad (14)$$

Only values $\epsilon_x = \epsilon_y = 0$ were used in this study. That is, only forward prediction-backward correction was investigated.

The stability of this method was investigated in detail by MacCormack and his results show that stability is assured if

$$|\nu| \leq 1 \quad (15)$$

where ν is the Courant number given by

$$\nu = \sigma \frac{\Delta T}{\Delta x}$$

and σ represents the eigenvalues of the Jacobian matrix $\partial F / \partial E$ which arises in the stability analysis of (6). The stability bound is derived

by noting that the absolute value of the eigenvalues of the amplification matrix must be less than one where the eigenvalues of the matrix are given by

$$\lambda_A = 1 - i\nu \sin \theta - \nu^2(1 - \cos \theta). \quad (16)$$

In the application of this method to the one-dimensional wave Eq. (10), the amplification factor of the scalar difference operator is given by (16) where the Courant number is written as $c\Delta T/\Delta x$.

It is instructive to consider the phase angle and amplitude of the one-dimensional amplification factor

$$\xi = 1 - i\nu \sin \theta - \nu^2(1 - \cos \theta).$$

The magnitude is given by

$$|\xi| = [1 - \nu^2(1 - \nu^2)(1 - \cos \theta)^2]^{1/2} \quad (17)$$

and the phase is given by

$$\phi = \tan^{-1} \frac{\text{Im}(\xi)}{\text{Re}(\xi)} = \tan^{-1} \left[\frac{-\nu \sin \theta}{1 - \nu^2(1 - \cos \theta)} \right] \quad (18)$$

As noted by Crowley (1968), the relative error in amplitude is given by $1 - |\xi|$ and the relative phase error is $1 - \phi/\theta\nu$ when the solution is advanced in time. Figure 1 presents contour plots of constant $|\xi|$ for values of ν and the reduced frequency θ/π . The contours shown in Fig. 2 are lines of constant $-\phi/\theta\nu$. These plots show that both phase and amplitude errors increase with θ/π for a given value of ν . The amplitude error is small at low values of ν . The amplitude error is small again at large values of ν . The phase error does just the

opposite. The amplification factor and the plots of amplitude and phase angle are the same as were presented for the Lax-Wendroff method by Crowley. The amplification factor for these two methods is identical.

Rusanov's Method Rusanov (1970) and Burstein and Mirin (1970) simultaneously developed a third-order scheme based on application of the Runge-Kutta method. Due to its recent development, this technique has not been as extensively applied to fluid flow problems as MacCormack's method. Taylor, Ndefv and Masson (1972) and Anderson and Vogel (1971) have presented comparative solutions using both Rusanov's and MacCormack's methods. They have concluded that the third-order method possesses greater flexibility in problems where larger variations in flow field properties occur. It should be noted that the results of those investigations were for shocked flows and represent relatively short computation times with large changes in the flow field dependent variables.

The third-order Rusanov method applied to the hyperbolic Eq. (6)

is

$$\begin{aligned}
 E_{j+1/2}^{(1)} &= \frac{1}{2} (E_{j+1}^n + E_j^n) - \frac{\Delta T}{3\Delta x} (F_{j+1}^n - F_j^n) \\
 E_j^{(2)} &= E_j^n - \frac{2}{3} \frac{\Delta T}{\Delta x} (F_{j+1/2}^{(1)} - F_{j-1/2}^{(1)}) \\
 E_j^{n+1} &= E_j^n - \frac{3}{8} \frac{\Delta T}{\Delta x} \left[-2F_{j+2}^{(1)} + 7F_{j+1}^{(1)} - 7F_{j-1}^{(1)} + 2F_{j-2}^{(1)} \right] \\
 &\quad - \frac{3}{8} \frac{\Delta T}{\Delta x} [F_{j+1}^{(2)} - F_{j-1}^{(2)}] \\
 &\quad - \frac{\omega}{24} [E_{j+2}^n - 4E_{j+1}^n + 6E_j^n - 4E_{j-1}^n + E_{j-2}^n]. \quad (19)
 \end{aligned}$$

This third-order method was developed using centered differences. The perfect shift condition is also satisfied for a Courant number of one and the proper choice of the ω parameter. The omega term in the third step is a fourth-order difference required for stability. Since it is fourth-order, the third-order accuracy of the method is unaffected by its addition.

The stability analysis of this technique has been carried out in detail by Burstein and Mirin (1970). Their results show that the stability of the system is assured if

$$|\nu| < 1$$

and

$$4\nu^2 - \nu^4 \leq \omega \leq 3 \quad (20)$$

The application of the Rusanov method to the linear Eq. (10) produces the amplification factor of the scalar difference operator which is

$$\begin{aligned} \xi = 1 - \frac{\nu^2}{2} \sin^2 \theta - \frac{2\omega}{3} \sin^4 \frac{\theta}{2} \\ - i\nu \sin \theta \left[1 + \frac{2}{3} (1 - \nu^2) \sin^2 \frac{\theta}{2} \right] \end{aligned} \quad (21)$$

Contour plots of phase and amplitude are presented in Figs. 3 and 4. An additional difficulty arises in presenting this data since the factor ω appears as a parameter free to take on values within the stability bounds given in (20). The only possible contours that can be constructed and interpreted are those for which $\omega = 3$. The lower bound on ω predicted by linear theory depends upon the Courant number. As a result, the curves for any value of ω less than 3 would violate the stability

bound over some range of $|\nu|$. Figure 3 presents the constant magnitude contours for $|\xi|$. In contrast to the second-order method, the largest damping occurs at midrange values of wave number while at both high and low wave numbers relatively little damping occurs. In comparing the second and third-order amplitude contours, it appears that little is gained by using the higher order. The phase error contours show an improvement.

These results are better understood if the modified equation produced by applying each method to the wave Eq. (10) is examined. Application of MacCormack's method to the linear wave equation results in the modified Eq.

$$\frac{\partial u}{\partial t} + \frac{c \partial u}{\partial x} = -\frac{1}{6} c \Delta x^2 (1 - \nu^2) \frac{\partial^3 u}{\partial x^3} + \dots \quad (22)$$

while the Rusanov equation becomes

$$\begin{aligned} \frac{\partial u}{\partial t} + \frac{c \partial u}{\partial x} = & -\frac{c}{24} \Delta x^3 \left[\frac{\omega}{\nu} - 4\nu + \nu^3 \right] \frac{\partial^4 u}{\partial x^4} \\ & - \frac{c}{120} c \Delta x^4 \left[5\omega - 4 - 15\nu^2 + 4\nu^4 \right] \frac{\partial^5 u}{\partial x^5} + \dots \end{aligned} \quad (23)$$

Kutler, Lomax and Warming observed that the lowest order term is the modified equation representing dispersion or phase error was a third derivative term in the second-order case while in the third-order method, the lowest order dispersive term is a fifth derivative. For both methods the lowest order even, or dissipative, term is a fourth derivative. One might expect that improvements in moving to the third-order technique should result from a decrease in phase error. This conclusion was verified by Kutler, Lomax and Warming (1972) for shocked flows.

Application to the case of non-shocked flows is discussed in a later section.

The Kutler-Lomax-Warming Method Kutler, Lomax and Warming (1972)

have developed a noncentered version of the Rusanov scheme. There are two major differences between their technique and the original third-order Rusanov method.

The K-L-W method uses noncentered differences and uses the MacCormack method (evaluated at $2/3\Delta T$) for the first two steps while the Rusanov third level is used. This results in less computer storage and computation time since only values at each mesh point are required. The other difference is that the fourth-order ω term has been differenced in a conservative manner so that the value of ω can be altered during the calculations. If the ω term is differenced as in the Rusanov method and altered during computation, incorrect wave speeds occur in the numerical solution.

The K-L-W method applied to the wave Eq. (6) takes the form

$$\begin{aligned}
 E_j^{(1)} &= E_j^n - \frac{2}{3} \frac{\Delta T}{\Delta x} \left[(1 - \epsilon) F_{j+1}^n - (1 - 2\epsilon) F_j^n - \epsilon F_{j-1}^n \right] \\
 E_j^{(2)} &= \frac{1}{2} \left[E_j^n + E_j^{(1)} \right] - \frac{1}{3} \left\{ \frac{\Delta T}{\Delta x} \left[\epsilon F_{j+1}^{(1)} + (1 - 2\epsilon) F_j^{(1)} + (\epsilon - 1) F_{j-1}^{(1)} \right] \right\} \\
 E_j^{n+1} &= E_j^n - \frac{\omega_{j+1/2}^n}{24} \left[E_{j+2}^n - 3E_{j+1}^n + 3E_j^n - E_{j-1}^n \right] \\
 &\quad + \frac{\omega_{j-1/2}^n}{24} \left[E_{j+1}^n - 3E_j^n + 3E_{j-1}^n - E_{j-2}^n \right] \\
 &\quad - \frac{1}{24} \frac{\Delta T}{\Delta x} \left[-2F_{j+2}^n + 7F_{j+1}^n - 7F_{j-1}^n + 2F_{j-2}^n \right] \\
 &\quad - \frac{3}{8} \frac{\Delta T}{\Delta x} \left[F_{j+1}^{(2)} - F_{j-1}^{(2)} \right] .
 \end{aligned} \tag{24}$$

The form of this method applied to the two dimensional sample problem reads:

$$\begin{aligned}
 A_{i,j}^{(1)} &= A_{i,j}^n - \frac{2}{3} \frac{\Delta T}{\Delta x} \left[(uA)_{i+1,j}^n - (uA)_{i,j}^n \right] - \frac{2}{3} \frac{\Delta T}{\Delta y} \left[(vA)_{i,j+1}^n - (vA)_{i,j}^n \right] \\
 A_{i,j}^{(2)} &= \frac{1}{2} \left\{ A_{i,j}^n + A_{i,j}^{(1)} - \frac{2}{3} \frac{\Delta T}{\Delta x} \left[(uA)_{i,j}^{(1)} - (uA)_{i-1,j}^{(1)} \right] - \frac{2}{3} \frac{\Delta T}{\Delta y} \left[(vA)_{i,j}^{(1)} - (vA)_{i,j-1}^{(1)} \right] \right\} \\
 A_{i,j}^{n+1} &= A_{i,j}^n - \frac{(\omega_x)^n}{24} \frac{i+1/2,j}{24} \left[A_{i+2,j}^n - 3A_{i+1,j}^n + 3A_{i,j}^n - A_{i-1,j}^n \right] \\
 &\quad + \frac{(\omega_x)^n}{24} \frac{i-1/2,j}{24} \left[A_{i+1,j}^n - 3A_{i,j}^n + 3A_{i-1,j}^n - A_{i-2,j}^n \right] \\
 &\quad - \frac{(\omega_y)^n}{24} \frac{i,j+1/2}{24} \left[A_{i,j+2}^n - 3A_{i,j+1}^n + 3A_{i,j}^n - A_{i,j-1}^n \right] \\
 &\quad + \frac{(\omega_y)^n}{24} \frac{i,j-1/2}{24} \left[A_{i,j+1}^n - 3A_{i,j}^n + 3A_{i,j-1}^n - A_{i,j-2}^n \right] \\
 &\quad - \frac{1}{24} \left\{ \frac{\Delta T}{\Delta x} \left[-2(uA)_{i+2,j}^n + 7(uA)_{i+1,j}^n - 7(uA)_{i,j}^n + 2(uA)_{i-2,j}^n \right] \right. \\
 &\quad \left. + \frac{\Delta T}{\Delta y} \left[-2(vA)_{i,j+2}^n + 7(vA)_{i,j+1}^n - 7(vA)_{i,j-1}^n + 2(vA)_{i,j-2}^n \right] \right\} \\
 &\quad - \frac{3}{8} \left\{ \frac{\Delta T}{\Delta x} \left[(uA)_{i+1,j}^{(2)} - (uA)_{i-1,j}^{(2)} \right] + \frac{\Delta T}{\Delta y} \left[(vA)_{i,j+1}^{(2)} - (vA)_{i,j-1}^{(2)} \right] \right\}
 \end{aligned} \tag{25}$$

where functionally

$$\begin{aligned}
 (\omega_x)^n_{i+1/2,j} &= \omega_x \left[(\nu_x^n)_{i+1/2,j} \right] \\
 (\omega_y)^n_{i+1/2,j} &= \omega_y \left[(\nu_y^n)_{i,j+1/2} \right]
 \end{aligned} \tag{26}$$

and

$$\begin{aligned}
 (\nu_x)^n_{i+1/2,j} &= \frac{1}{4} \left[(\lambda_x)^n_{i+2,j} + (\lambda_x)^n_{i+1,j} + (\lambda_x)^n_{i,j} + (\lambda_x)^n_{i-1,j} \right] \frac{\Delta t}{\Delta x} \\
 (\nu_y)^n_{i,j+1/2} &= \frac{1}{4} \left[(\lambda_y)^n_{i,j+2} + (\lambda_y)^n_{i,j+1} + (\lambda_y)^n_{i,j} + (\lambda_y)^n_{i,j-1} \right] \frac{\Delta t}{\Delta y}
 \end{aligned}
 \tag{27}$$

This method has the same stability bounds and magnitude as the Rusanov method and phase angle plots shown in Figs. 3 and 4 for Rusanov's method are applicable.

Kutler, Lomax and Warming observed that this third-order method usually produced better results in problems involving large changes in the dependent variables than did second-order techniques. However, some sensitivity of the results to variations in the local eigenvalue structure led them to attempt to "tune" the method at each step by changing the value of the ω parameter.

Application of the K-L-W method to the simple wave Eq. (10) results in the modified differential Eq. (23) common to third-order Runge-Kutta methods. To reduce the dissipation of the method, the ω parameter should be selected to minimize the fourth derivative term. If the coefficient of this term is set equal to zero then

$$\omega = 4\nu^2 - \nu^4 \tag{28}$$

which is lower stability bound as predicted by linear theory. If minimum dispersion is desired, the coefficient of the fifth-order term is set equal to zero giving

$$\omega = \frac{(4\nu^2 + 1)(4 - \nu^2)}{3} \tag{29}$$

Results presented by Kutler, Lomax and Warming (1972) show that an improvement in the solution is achieved if ω is altered according to either of these schemes. It should be noted that the value of ν appearing in (28) and (29) is the local value of the Courant number. The ω_x and ω_y of (26) are thus determined through (28) and (29) with the appropriate values of ν given in (27).

The amplitude and phase error contour plots for the variable ω cases are presented in Figs. 5 through 8. The minimum dissipation amplitude plot in Fig. 5 shows that the "tuned" third-order method is less dissipative than the second-order technique. The effect of changing ω to eliminate the first even term in the modified equation clearly reduces the damping. This should be compared with Fig. 7 which is also an amplitude contour plot but for minimum phase error as provided with ω determined through (26). It is apparent that the damping is greater in this case but only below Courant numbers of about 0.6. This should have been anticipated since the allowable range of ω is restricted at higher Courant numbers and the method becomes less sensitive to the value of ω used.

The phase angle contours show that the minimum dispersion case in Fig. 8 provides a smaller phase error over the entire range of stable values of ν than the minimum dissipation case shown in Fig. 6. On the basis of the amplitude and phase angle plots one would expect results using the "tuned" K-L-W method to be superior to the constant ω third-order methods. Application to a problem justifying this conclusion is presented in the following section.

3. Numerical Calculations

A simple velocity field is prescribed over a coordinate mesh if it is assumed that it is produced by solid body rotation about some axis. In this case the divergence of the velocity field is zero and the conservative form given in (3) is valid. The initial distribution of A is chosen to be a cone of unit altitude at the center decreasing to zero at the base radius of four cell widths. The following data were held constant during the calculations unless otherwise noted:

n = number of time steps = 40

Ω = rigid body angular velocity = - .001 radians/sec

Δt = time step = 30 seconds

$\Delta x = \Delta y = \Delta = 1.0$ = mesh size

Center of rotation (12, 12)

Center of initial A distribution (18, 12).

A schematic representation of this problem is shown in Fig. 9.

Figure 10 presents the results of using MacCormack's method with a forward predictor, backward corrector while the results obtained with a backward predictor, forward corrector are shown in Fig. 11. The results in both cases are similar in terms of correctly advecting the center of the disturbance and in reproducing contours of constant A. The results are very similar to those produced using the Lax-Wendroff method as reported by Fattahi (1971).

The Rusanov third-order method using $\omega = 3$ was applied to this problem and the results are shown in Fig. 12. These results are not very encouraging. However, a more detailed analysis of the situation produces some important information. The Rusanov method has been shown to produce

results which are unfavorable when the Courant number is not close to one and the upper limit value of 3 is used for ω . In this problem the mesh ratio is $\Delta T/\Delta = 30$ which gives an effective Courant number of approximately 0.35 based on the maximum velocity. This means that the local Courant number at each point in the mesh is less than or equal to 0.35. Referring to Figs. 3 and 4, the most dissipative and dispersive regions of the Rusanov method lie in this range. This is the reason for the poor results shown in Fig. 12. It is interesting to note that the MacCormack method provides a better solution for this case than the third-order Rusanov technique. Figs. 1 and 2 show that less dissipation and dispersion are introduced in the solution using the MacCormack method for the range of effective Courant numbers encountered in this numerical example. For this case the minimum value of ω for stability required by the Rusanov method is approximately 0.5 while the maximum value is 3. Calculations using values of ω near the lower bound have resulted in good solutions for problems involving shocked flows like those of Kutler, Lomax and Warming (1972) and also for the sample problem presented here by Burstein and Mirin (1970) and Fattahi. Values of ω near or below the linear stability bound result in excellent solutions for shocked flows. Fattahi (1971) reports a similar conclusion and, in solving the exact problem as presented here, notes that an ω value of about 0.6 produces the best results. This is shown in Fig. 13. Solutions obtained with ω below the linear stability bound provide excellent results for short integration times. For long integration times the solution eventually becomes unstable if a value of ω outside the allowed range is used.

The problem of selecting the proper value of ω is alleviated if the Kutler-Lomax-Warming technique with either minimum dispersion or dissipation is used. Figures 14 and 15 present the results of these calculations for a time step of $\Delta T = 30$ seconds. The minimum dissipation case provides better results at this value of ΔT . Referring to the amplitude contours for these two methods reveals that the damping is severe for the minimum dispersion case at low Courant numbers. This is apparent if the maximum advected value is compared for these two cases. This type of problem is evidently more sensitive to dissipative errors than errors in phase angle. Kutler, Lomax and Warming (1972) concluded that the minimum dispersion provided better results for their work involving shocked flows. The difference in the results using the two ways of calculating ω diminishes as the linear stability bound is approached. Solutions for a time step of $\Delta T = 75$ sec are shown in Figs. 16 and 17. As noted from the damping and phase error curves, the results obtained should be similar. However, the minimum dissipation solution still appears to be more satisfactory.

4. Conclusions

A comparison of relative errors and computation times are presented in Table 1. Based on accuracy in terms of maximum advected value, phase error and error in the radius of the center location, the third-order methods are usually better unless relatively low values of Courant number are coupled with large values of ω . The third-order methods require the same magnitude of computer time as MacCormack's method. They are still an order of magnitude faster than the fourth-order space,

second-order time Roberts and Weiss method. Although this technique was not investigated here, Molenkamp (1968) has reported the relative time required for its use.

Of the methods tested, the Kutler-Lomax-Warming method tuned for minimum dissipation provides the best comparison with the exact solution. This method should be studied in more detail. In particular results using the various combinations of the ϵ 's defined in (14) should be compared. The results reported here used a forward predictor and backward corrector to advance to $2/3\Delta t$ and central differencing in the third step. In addition, application should be made to more complex problems to assess the usefulness of the technique of altering the stability parameter ω during the computation. While the eigenvalue structure required in choosing the proper ω in a complex problem is difficult, reasonable approximations can be made. The increase in accuracy of the resulting solution far outweighs the additional effort.

Acknowledgments

This research was supported by the Iowa State University Engineering Research Institute, Ames, Iowa, through funds made available by NASA grant NGR 16-029.

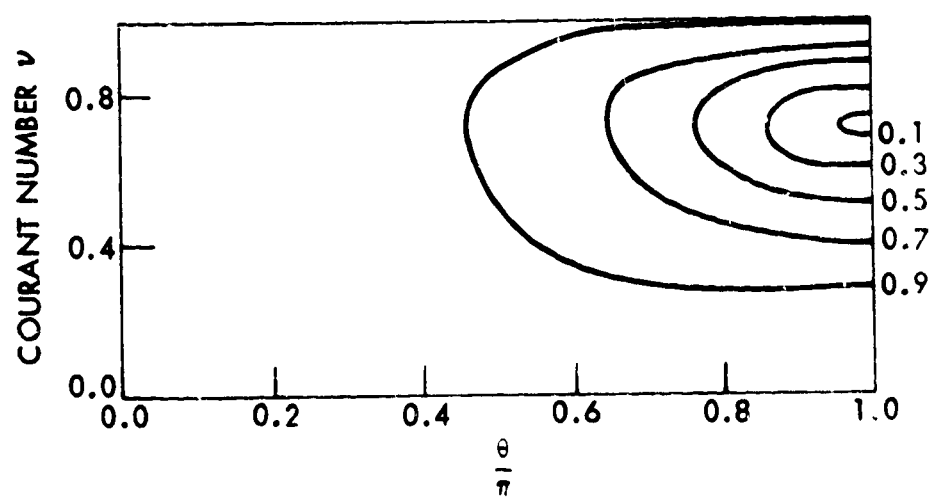
References

- D. A. Anderson and J. M. Vogel, July 1971, "Numerical Solutions of Flow Fields Behind Rectangular Wings," Engineering Research Institute Report ERI-71015, Iowa State University, Ames, Iowa.
- Samuel A. Burstein and Arthur A. Mirin, June 1970, "Third-Order Difference Methods for Hyperbolic Equations," J. Comp. Phys., Volume 5, No. 3, 547-571.
- W. P. Crowley, January 1968, "Numerical Advection Experiments," Monthly Weather Review, Volume 96, No. 1, 1-11.
- Behrooz Fattahi, 1971, "Application of Conservative Finite-Difference Methods to Advection Problems," Unpublished Master of Engineering Paper, Iowa State University.
- Paul Kutler, Howard Lomax, and R. F. Warming, 1972, "Computation of Space Shuttle Flow Fields Using Noncentered Finite-Difference Schemes," AIAA Paper, 72-193.
- R. W. MacCormack, 1967, "The Effect of Viscosity in Hypervelocity Impact Cratering," AIAA Paper, 69-354.
- R. W. MacCormack, 1971, "Numerical Solution of the Interaction of a Shock Wave with a Laminar Boundary Layer," Proc. Second Intern. Conf. on Numerical Methods in Fluid Dynamics, edited by M. Holt, Berlin, Springer-Verlag, 151-163.
- Charles R. Molenkamp, April 1968, "Accuracy of Finite-Difference Methods Applied to the Advection Equation," J. Appl. Meteor., Volume 7, No. 5, 160-167.
- K. Roberts and N. Weiss, 1966, "Convective Difference Schemes," Mathematics of Computations, Vol. 20, No. 94, 272-299.
- V. V. Rusanov, June 1970, "On Difference Schemes of Third-Order Accuracy for Nonlinear Hyperbolic Systems," J. Comp. Phys., Vol. 5, No. 3, 507-516.
- T. D. Taylor, E. Ndefv, and B. S. Masson, February 1972, "A Study of Numerical Methods for Solving Viscous and Inviscid Flow Problems," J. Comp. Phys., Vol. 9, No. 2, 99-120.

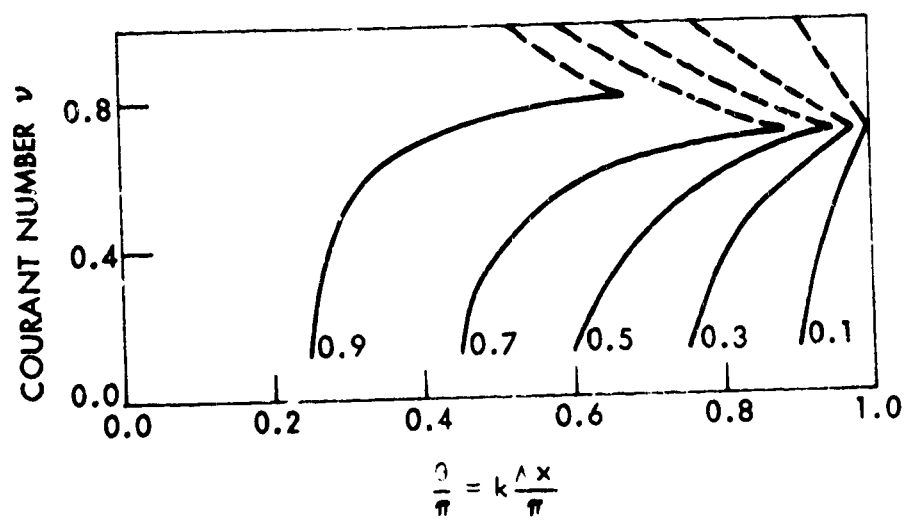
Table 1. Comparison of Calculated Results

Type	Maximum at a Grid Point	Angular displacement error (% of total rotation)	Radial displacement error (% of radius)	Relative computation time
MacCormack (forward predictor, backward corrector)				
$\Delta T = 30$	0.816	- 7.270	-2.440	1
MacCormack (backward predictor forward corrector)				
$\Delta T = 30$	0.862	- 7.270	- 2.440	1
Rusanov				
$\Delta T = 30, \omega = 3$	0.563	1.452	- 2.440	2.200
$\Delta T = 30, \omega = 0.6$	0.777	0	- 1.600	2.345
Kutler-Warming-Lomax minimum dissipation				
$\Delta T = 30$	0.871	0	- 1.625	1.642
$\Delta T = 75$	0.882	0	- 1.625	0.804
Minimum dispersion				
$\Delta T = 30$	0.738	0	- 1.625	1.735
$\Delta T = 75$	0.821	0	- 1.625	0.810

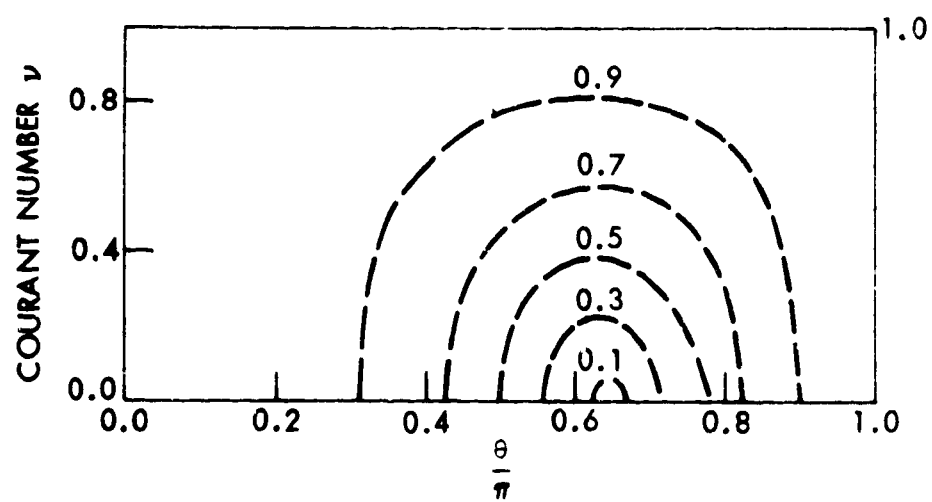
- Fig. 1. Constant $|\xi|$ contour for MacCormack's second order method.
- Fig. 2. Contour of $-\phi/\theta\alpha$ for MacCormack's second order method.
- Fig. 3. Constant $|\xi|$ contours for Rusanov Method with $\omega = 3.0$.
- Fig. 4. Phase angle for Rusanov Method with $\omega = 3.0$.
- Fig. 5. Constant $|\xi|$ contours for K-L-W Method for minimum dissipation.
- Fig. 6. Relative phase error for the K-L-W Method tuned for minimum dissipation.
- Fig. 7. Constant $|\xi|$ contours for the K-L-W Method with minimum dispersion.
- Fig. 8. Contours of $-\phi/\theta\alpha$ for K-L-W Method with minimum dispersion.
- Fig. 9. Schematic representation of the advection problem showing the initial A distribution.
- Fig. 10. Solution using the MacCormack (forward predictor, backward corrector) Method.
- Fig. 11. Solution using the MacCormack (forward predictor, backward corrector) Method.
- Fig. 12. Solution using Rusanov's Method with $\omega = 3.0$.
- Fig. 13. Solution using the Rusanov-Burstein-Mirin Method, $\omega = 0.6$, $\Delta T = 30$.
- Fig. 14. Solution using the K-L-W Method tuned for minimum dissipation $\Delta T = 30$ sec.
- Fig. 15. Solution using the K-L-W Method tuned for minimum dispersion $\Delta T = 30$ sec.
- Fig. 16. Solution using the K-L-W Method tuned for minimum dissipation $\Delta T = 75$ sec.
- Fig. 17. Solution using the K-L-W Method tuned for minimum dispersion $\Delta T = 75$ sec.



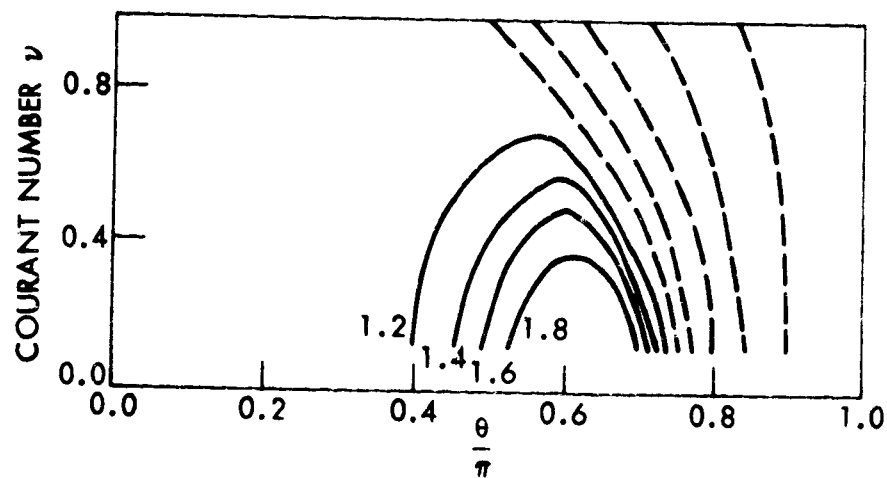
Anderson
Fig. 1



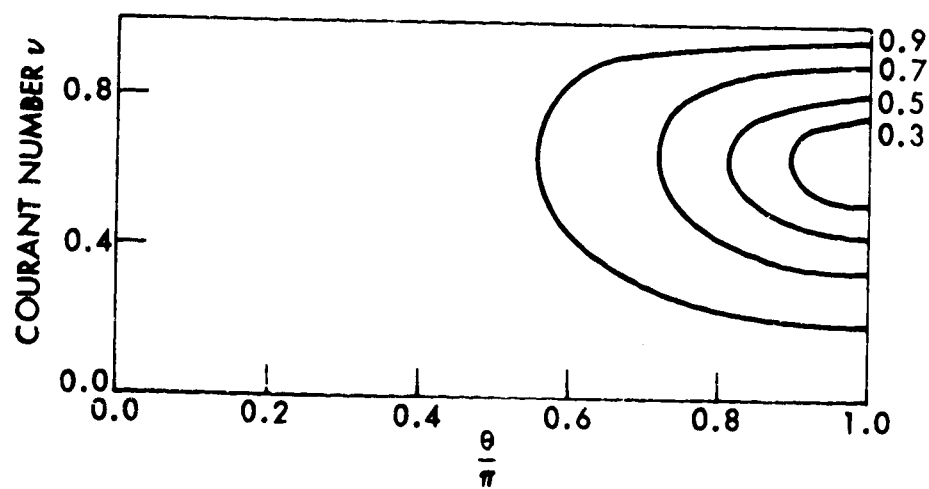
Anderson
Fig. 2



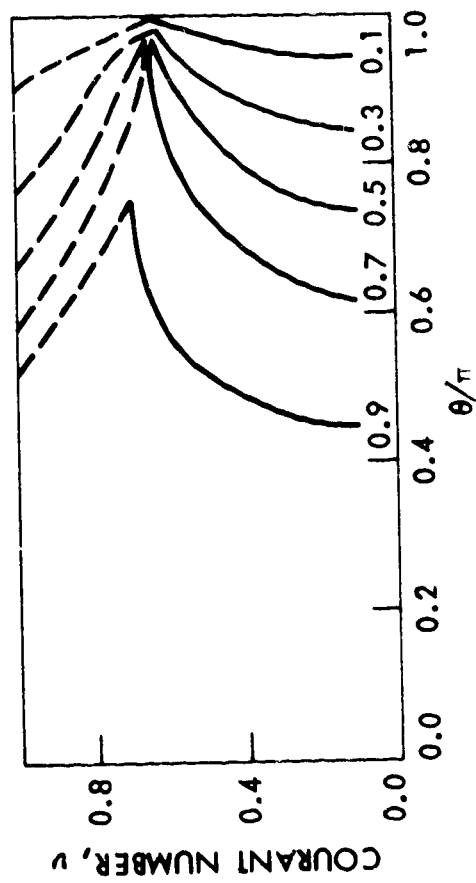
Anderson
Fig. 3



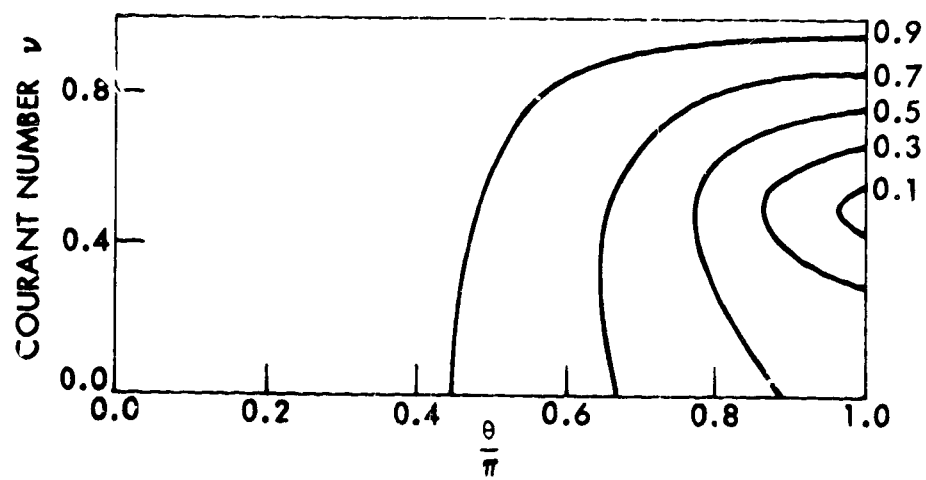
Anderson
Fig. 4



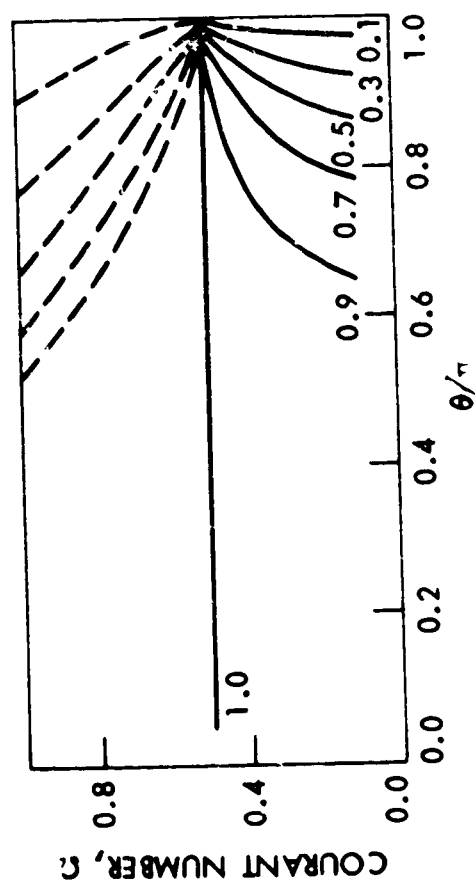
Anderson
Fig. 5



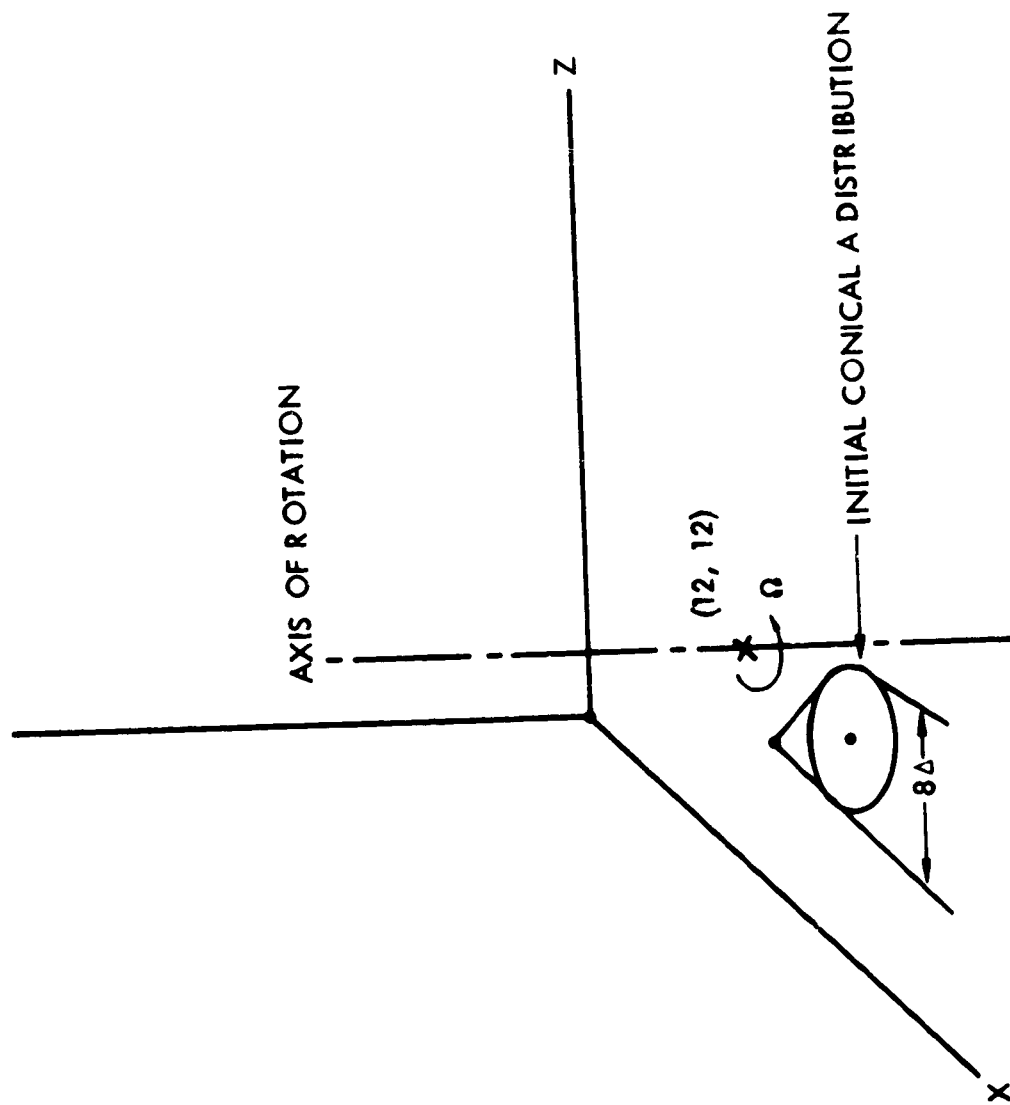
Anderson
Fig. 6



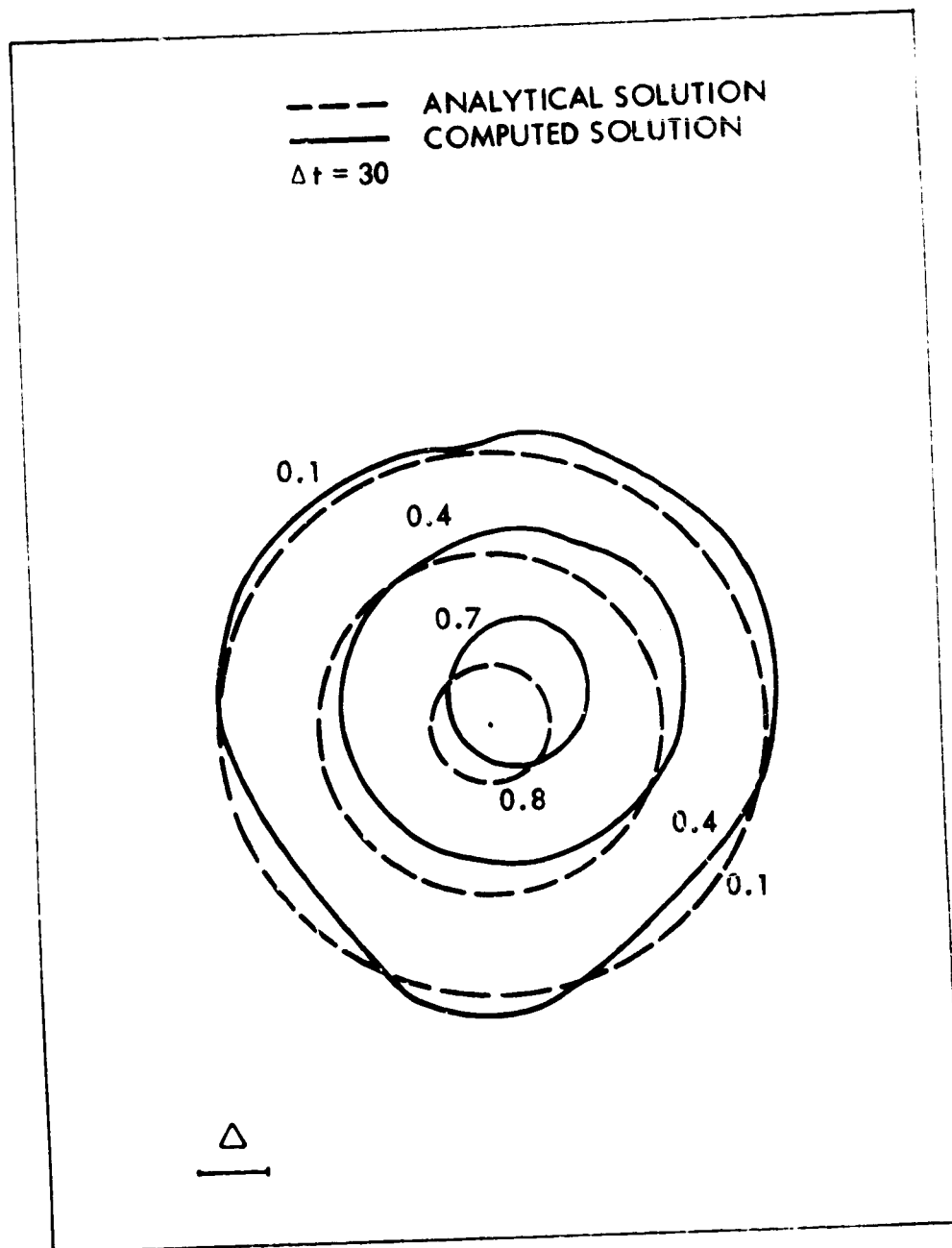
Anderson
Fig. 7



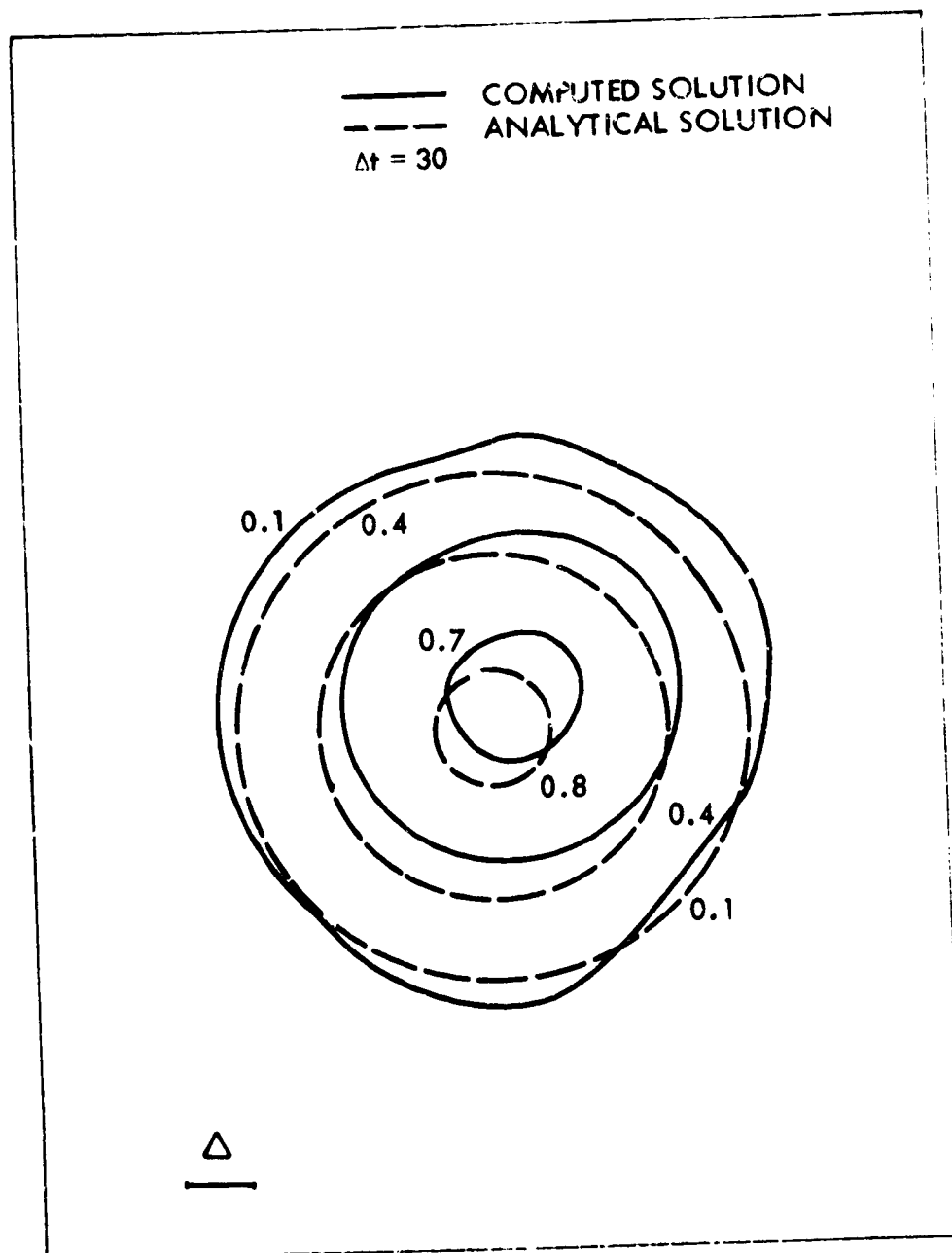
Anderson
Fig. 8



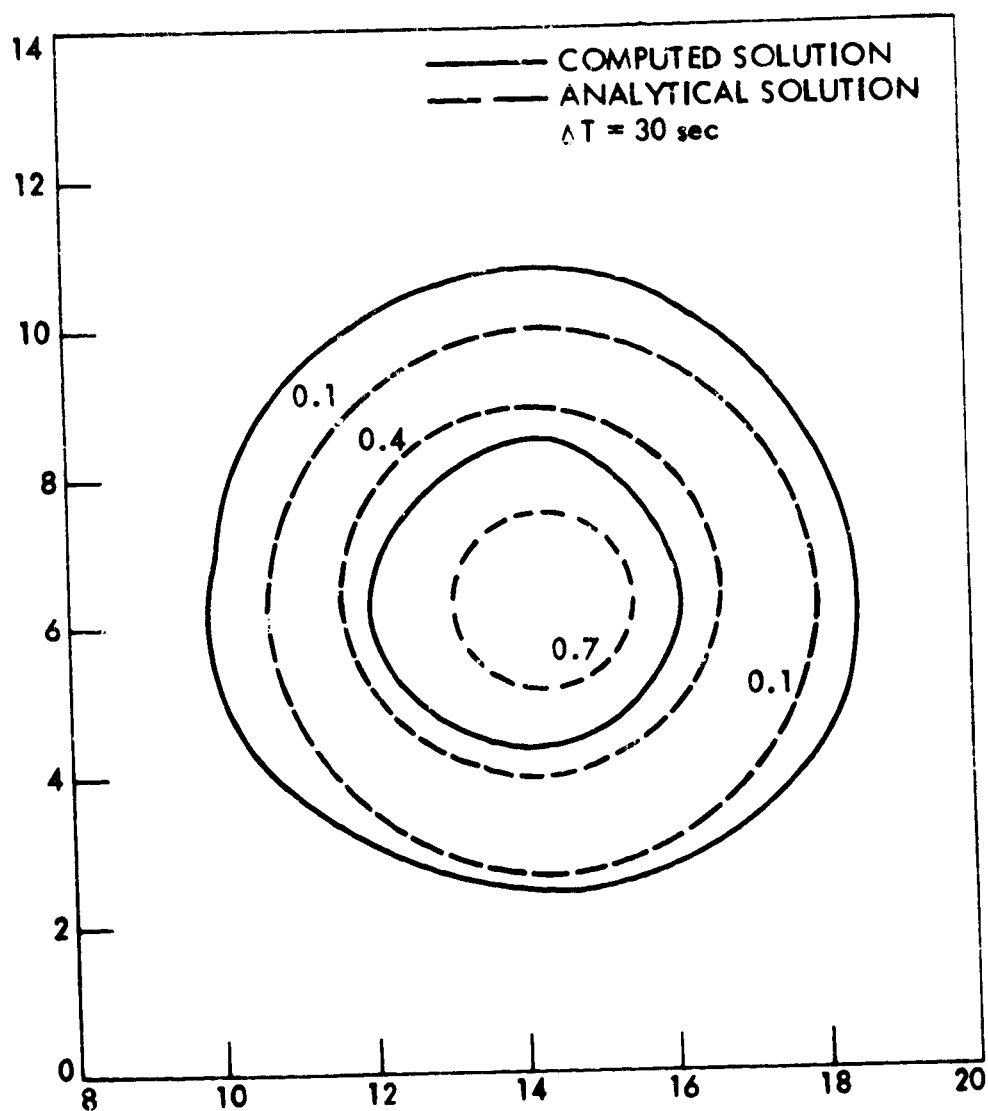
Anderson
Fig. 9



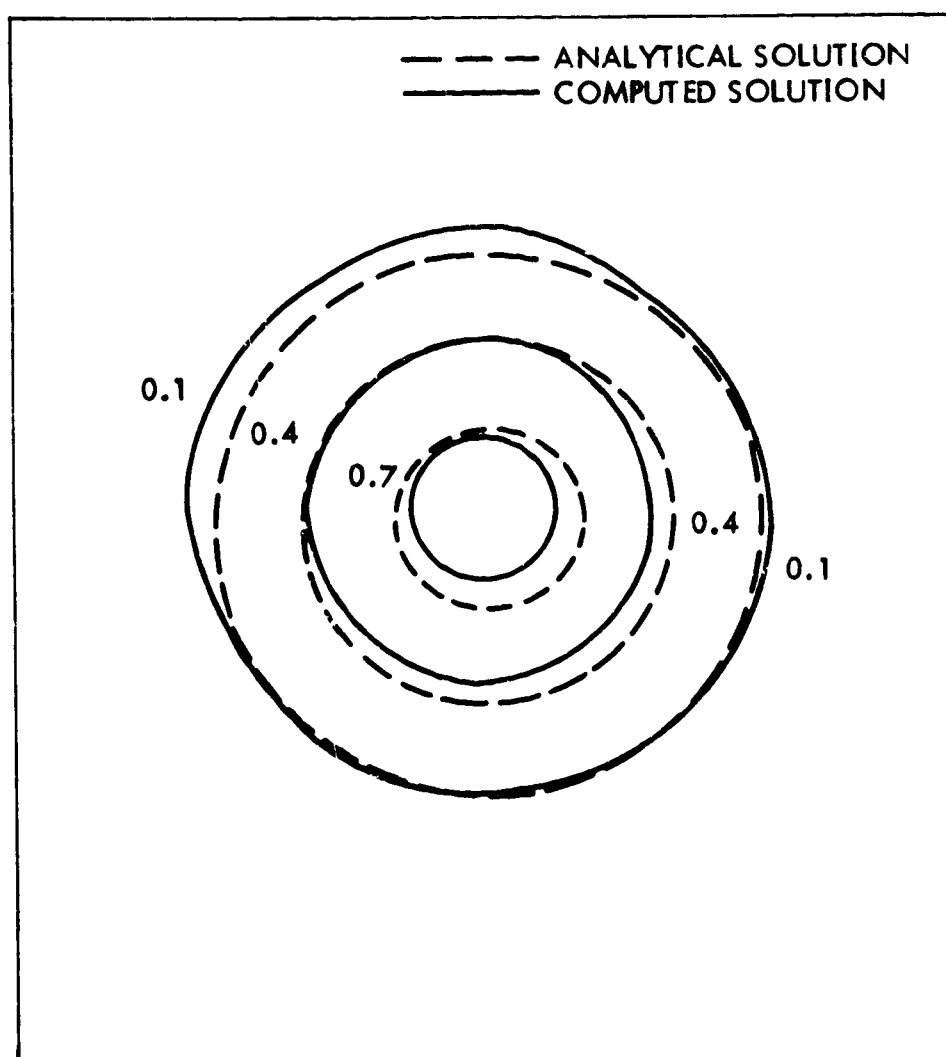
Anderson
Fig. 10



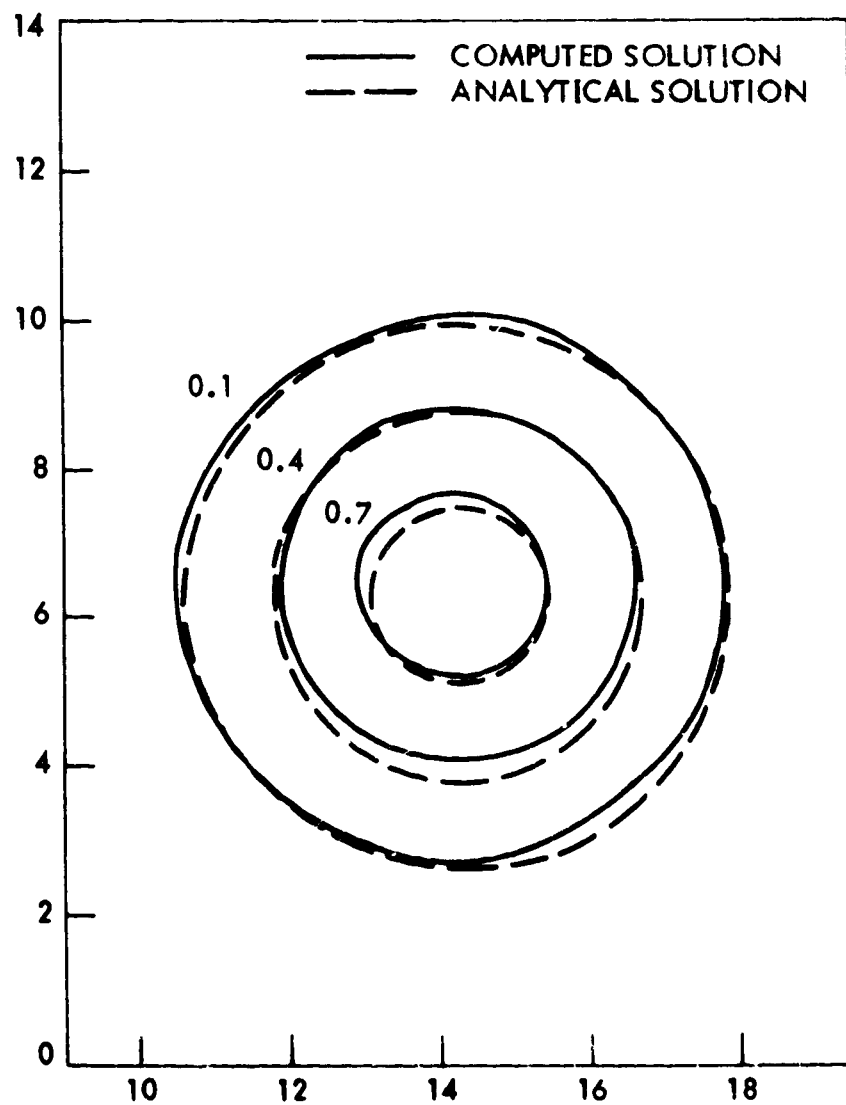
Anderson
Fig. 11



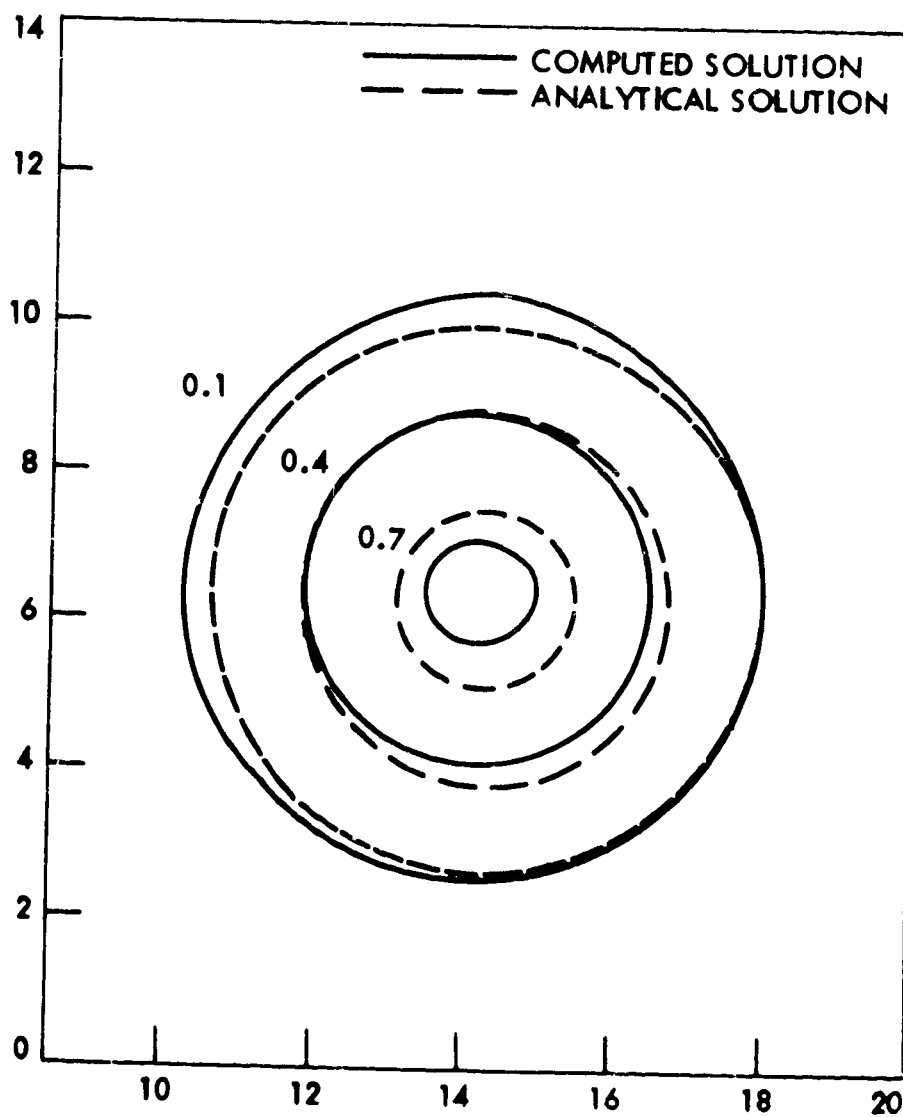
Anderson
Fig. 12



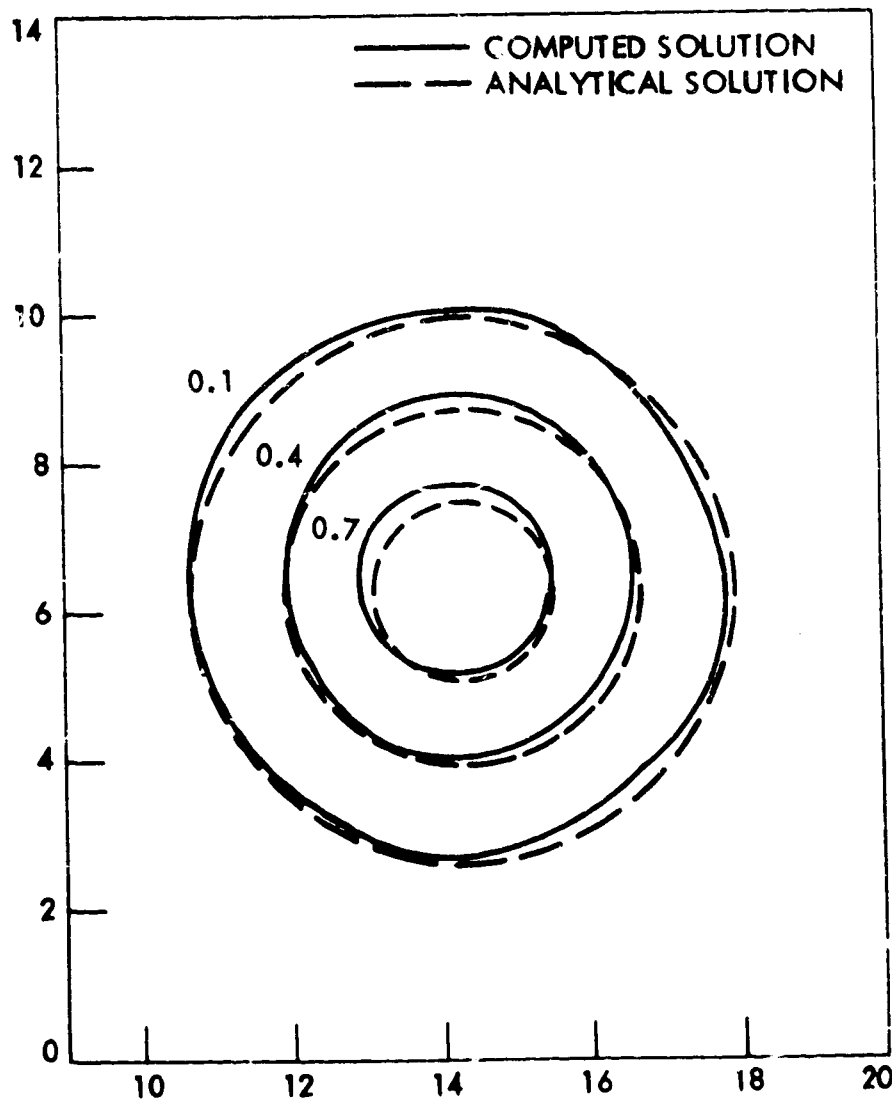
Anderson
Fig. 13



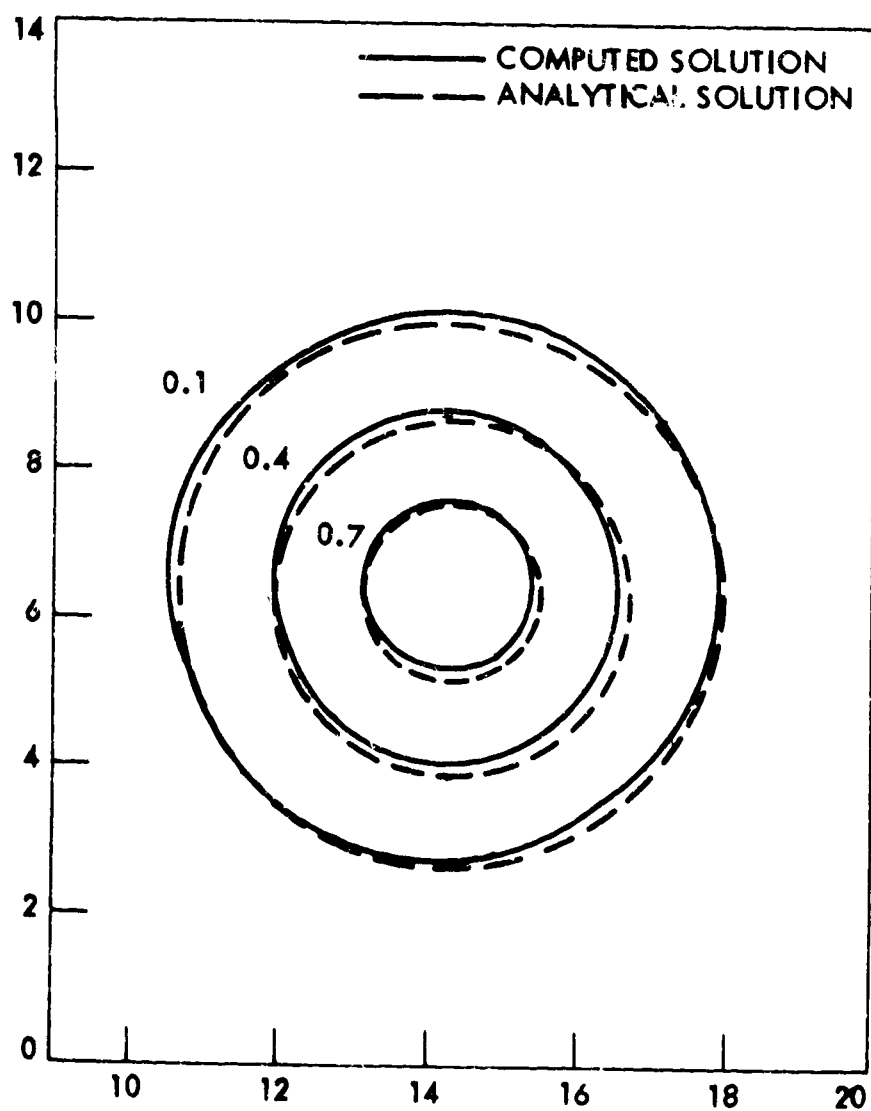
Anderson
Fig. 14



Anderson
Fig. 15



Anderson
Fig. 16



Anderson
Fig. 17

**END
DATE
FILMED**

JAN 15 1973